Fabrication, characterisation and analytical modelling of gradient auxetic closed cell foams

Olly Duncan[1*], Andrew Alderson[2], Tom Allen[1]

[1] *Department of Engineering, Faculty of Science & Engineering, Manchester Metropolitan University, John Dalton Building, Chester Street, Manchester M1 5GD, UK.*

[2] *Materials and Engineering Research Institute, Faculty of Science, Technology and Arts, Sheffield Hallam University, Howard Street, Sheffield S1 1WB UK.*

* Corresponding author (Email: O.Duncan@mmu.ac.uk)

Abstract

Auxetic (negative Poisson's ratio) and gradient open cell foams have shown promise for their conformability and high impact energy absorption – useful in applications like protective equipment, footwear and prosthetics. Recent methods fabricated closed cell auxetic foam by steaming conventional closed cell foam. Methods developed herein control the cell structure of auxetic closed cell foam, to produce novel intentionally anisotropic and gradient auxetic closed cell foam. Pins passed through the foam constrained or stretched regions during steaming to further modify cell structure and impart gradients in cell structure, Young's modulus and Poisson's ratios. Fabricated foams had Poisson's ratios between 1 and -1. Imparted Young's moduli of 1 to 12 MPa were similar to foams used in footwear, prosthesis, helmets and other impact protection. The effect of changes to cell structure on Young's moduli and Poisson's ratio are explained by combining analytical models of auxetic open cell and conventional closed cell foam.

Keywords

negative Poisson's ratio, gradient, foam, impact protection, steam processing

1. Introduction

Auxetic foam has a negative Poisson's ratio (NPR; expanding transversely when stretched and contracting transversely when compressed) [1]. NPR can increase conformability [2,3], indentation resistance [4,5], impact energy abortion [6–8], vibration damping [9–11], acoustic [12–14] and thermal insulation [15,16] and shear modulus [17,18], while also causing biaxial expansion and domed curvature [19,20]. Auxetic open cell foams, with established fabrication methods [1,21,22], have been proposed and tested for a range of applications, including in prosthetic devices [19,23], seating [24], footwear [25], vibration limiting gloves for use in construction [11], crash barriers and pads [24,26], sports helmets [27] and other personal protective equipment [8,26,28]. Most auxetic foam research focusses on open cell foam with Young's modulus below ~0.2 MPa [29,30]. A recent study produced low porosity open cell foam sheets with planar NPR in tension, and through thickness Young's moduli up to 25 MPa [31]. Personal protective equipment generally uses porous closed cell foam, containing trapped gas or air to increase the stiffness provided by the foam cell structure to between 1 and 20 MPa [32–34]. Without established methods to fabricate porous auxetic foams with desirable stiffness, products containing auxetic foams are not common.

Typical auxetic open cell foam fabrications first compress conventional thermo-plastic open cell foam, buckling cell ribs to impart a re-entrant like cell structure, which is commonly associated with NPR [1,21,22]. Heating and cooling cycles can then fix the imposed structure over time, so these fabrications are known as thermo-mechanical fabrications [1,21,35]. Solvents or gases can also be used as softening agents [22,36,37]. Anisotropic auxetic open cell foams can be made by applying different levels of compression in different directions [6,31,38]. Thermo-forming with curved moulds can also produce curved auxetic open cell foam [39]. Thermo-forming recently produced foam sheets with tensile NPR in both planar directions. The foam was highly compressed through thickness during thermo-forming, reducing through thickness porosity while imparting Young's modulus up to 25 MPa and positive compressive Poisson's ratio [31].

Gradient foams have different cell structures, Young's moduli and Poisson's ratio in pre-defined regions, and gradients can be discrete or continuous [19,23,40]. During open cell auxetic gradient foam fabrications, compression can be controlled, and hence varied, by passing pins through the foam sample, or by using a foam sample with a different shape to the mould [19,23,40]. Applying different compression regimes to different foam regions during fabrication can produce gradient open cell auxetic foams. Stretching foams in one or more directions by passing pins through the foam during fabrication produces long, re-entrant cells, increasing Young's modulus and the magnitude of positive or negative Poisson's ratio during loading parallel to the long cell axis [38,40,41]. Foam in personal protective equipment is often segmented so it fits the body better than a continuous sheet [42–44], but any reduction or loss of padding between segments may reduce protection. Varying material properties in running shoe midsole regions can influence and improve running style [45]. Gradient foams may offer benefits to personal protective equipment and footwear in terms of how they comfortably cover, deform with and protect body segments [19,23,40].

Chan and Evans found thermo-mechanical fabrications to rupture closed cell foam walls during fabrication [21,46]. Fabrication methods for auxetic closed cell foams that do not rupture cells use hydrostatic compressive pressure applied by a pressure vessel [47], or steam absorption and condensation [48,49]. Cell structure, Poisson's ratio and Young's moduli of closed cell auxetic foams vary with compression imparted following fabrication, with common volumetric compression ratios (original/final volume) being between 1.3 and 6.0 [47–49]. Of the two available options for fabricating closed cell auxetic foam, the steam fabrication method uses simpler equipment, such as a steam bath or an oven and a water filled container [48,49]. Upon cooling, as the foam shrinks and cell walls become re-entrant, the constituent polymer in some foams, such as polyethylene, passes through a thermal transition that fixes the imposed cell structure [48,49]. Absorbed water can, then, evaporate from the foam within a week of fabrication, leaving a stable auxetic closed cell foam with negligible trapped water [48,49].

Auxetic and conventional closed cell foam characteristics have been explained using dimensions estimated from two-dimensional (2D) projections of cell structures, based on microscopic imaging. Analytical models for conventional and auxetic foam consider the stretching, flexing and hinging of cell ribs to predict Poisson's ratios and Young's moduli [40,41,50]. No analytical model has been published considering infrequently researched auxetic closed cell foams. Analytical models for conventional closed cell foams have combined the effects of gas pressure on cell rib and wall deformation, estimating dimensions and orientations from 2D cell projections [41,51,52].

Auxetic closed cell foam fabrications that rely solely on pressure differentials offer limited control over compression [47–49]. As such, before beginning a study fabricating a new type, size or shape of auxetic closed cell foam, pilot work is needed to find the processing conditions that give the desired volumetric compression. Gradient or intentionally anisotropic auxetic closed cell foams have not previously been produced. This work explores two steam fabrication-based methods to control cell structure modification in different axis and foam regions. These fabrication methods were: i) Constraining or stretching foam regions, using pins, to produce intentionally anisotropic gradient foam, and ii) Preventing steam from reaching regions of a sample, to produce gradient foam. The effect of these methods and modifications to cell structure, on Young's modulus and Poisson's ratio, are explained by combining analytical models for open cell auxetic foam [40] and the effect of gas pressure in closed cell foam [51,52].

2. Methods

2.1. Fabrication

Two sheets (210 ×110 × 10 mm) and two cuboids (200 × 20 × 10 mm) of closed cell foam (Plastazote LD-60, algeos.com), pre-conditioned for a week in an environmental chamber (20°C and 10% relative humidity), were fabricated by steam processing [48,49]. One sheet of foam was unconstrained during fabrication. The other sheet was constrained at one end by twelve steel pins (Ø2 mm) passed through holes in aluminium plates (100 × 100 × 2 mm), sandwiching but not compressing the foam (Figure 1a). Pins were inserted in each corner and along each side of the plates with 33 mm spacing. The central 45 mm of one cuboid (i) was stretched to 1.5 times its original length, using four pins passed through the foam and an aluminium box section (surrounding but not touching) to hold the pins apart (2 mm thick walls, 22 × 22 × 65 mm Figure 1b). Foam samples and constraining devices were placed in 250 × 350 × 40 mm aluminium dishes (2 mm thick walls) filled to ~30 mm with water and covered with aluminium foil [49]. Cuboid (ii) was positioned with half its length inside an aluminium drinks can (Ø70 mm, height 100 mm, 1 mm wall thickness), filled to 80% with water, and with a ~15 × 15 mm hole in the top. The foam was passed through the hole in the can, so the upper half was dry heated during fabrication (Figure 1c).

All containers were heated in an oven (MCP Tooling Technologies LC/CD, +/- 0.25°C) set to 105°C for 4.5 hours [49]. After steaming, samples and constraining devices were removed from the containers and cooled for 30 minutes on a drying rack in an air-conditioned laboratory with an expected temperature of 20 to 25°C and relative humidity of 30 to 60%. Samples began to shrink upon removal from the water, with shrinking appearing to finish within 1 to 2 minutes. Constraining devices were then removed, and samples were returned to the environmental chamber for a week before testing. The order of cutting (Figure 1d), and testing, is shown in Figure 1e (tensile tests, then compression tests or micro-ct). Samples were returned to the environmental chamber between tests. Tests were in the air-conditioned laboratory described above (20 to 25°C and relative humidity of 30 to 60%).

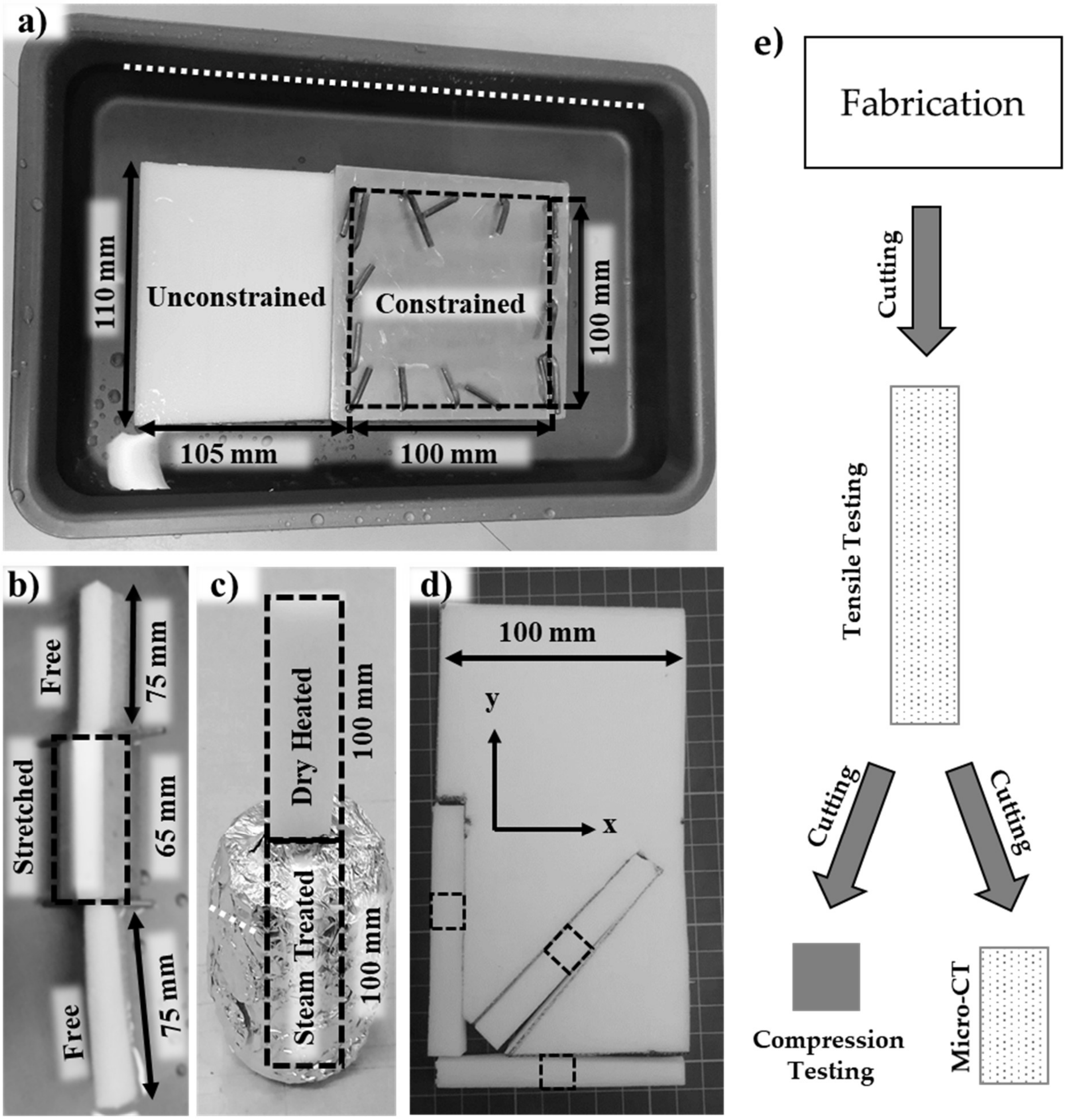

Figure 1. a) Sample containing constrained region (note the 5 mm edge surrounding the constrained region); b) Sample containing stretched region; c) Sample half steamed and half dry heated; d) Example tensile cuboids and compression (dashed lines) with sample orientations, locations and axis labelling marked; e) Order of sample preparation. The same orientations and co-ordinate systems were used for all sheets/regions. Y-axis parallel to sample length, x to width in (b) and (c). White dotted lines in (a) and (c) show water level.

2.2. Characterisation

Mass (Sartorius, M-power) and dimensions (Vernier Calipers) of all samples and regions were measured before and one week after fabrication, to see if any cells contained water, which would increase mass, and to measure linear compression ratios in each orthogonal axis (LCR, final/original length). The partially open cells on the faces of foam samples do not shrink during fabrication as they cannot trap steam [48,49]. Therefore, 1 to 2 mm was cut from the planar edges of converted samples with a utility knife (Stanley) before characterisation. The top and bottom faces were not removed, as samples were already thin (3 to 5 mm). Three samples of unconverted foam (100 × 10 × 10 mm), foam from the unconstrained sheet and from each region of the gradient sheet (~60 × 5 × 5 mm) were cut for tensile tests, with the utility knife, at 45° increments (Figure 1d). The two cuboids were cut for tensile testing, with one ~60 × 5 × 5 mm sample taken from each region (three samples in Figures 1b and two in c). The dimensions and mass of the tensile samples were used to calculate final density ratio (FDR, final/original density).

A speckle pattern was applied to all samples (matt Acrylic spray paint, Halfords) for full-field strain measurement using 2D digital image correlation (DIC). Tensile tests were at a strain rate of 0.0033 s^{-1} to 10% tension on an Instron 3369 with a 500 N load cell sampling at 25 Hz. Samples were clamped ~10 mm from their ends in the jaws of the device, which were closed to 1 mm, giving gauge lengths of 40 to 80 mm. These cuboidal samples had longer gauge lengths (>35 mm) and were thinner than the 12 mm sided 'dog-bone' samples specified in ASTM D3574 – 11, to account for end effects [53]. Tensile tests were filmed with a camera (**Figure 2a**), with its image plane aligned to a face of the sample (LaVision DIC package, 1260 × 1080 p, 10 fps, Nikon lenses with 100 mm optical zoom). A target area was defined over the central lengthwise third of samples (Figure 2b & c), giving axial and transverse true strains, with facet sizes set to give at least three speckles per facet (10 to 15 pixels) [54]. Device jaws were rotated 90° around the loading axis between tests, with the sample in place, to apply strain mapping to four faces. Sample cross sectional areas were measured before each test with Vernier Calipers to allow stress to be calculated.

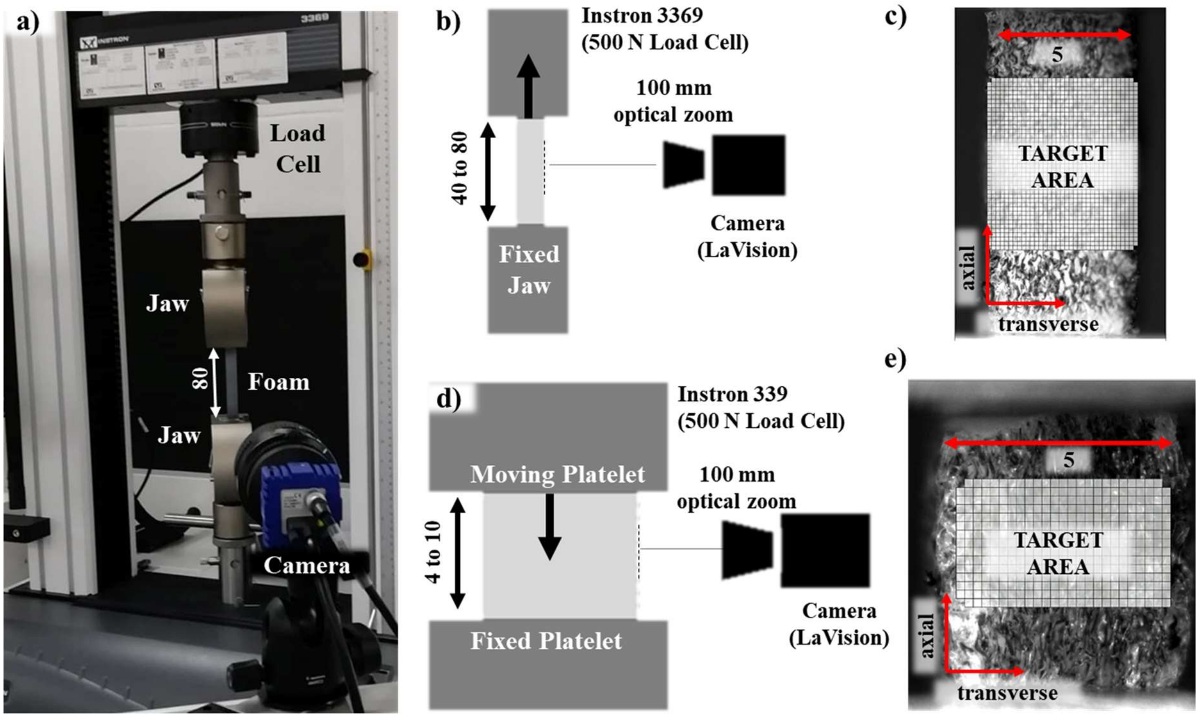

Figure 2. a) Tensile sample and camera, b) Tensile test schematic; c) tensile sample with speckle pattern and target area; d) compression test schematic; e) compression tests sample with speckle pattern and target area. Dimensions in mm.

Cubes for compression testing (4 to 10 mm sided) were cut from the lengthwise centre of all tensile samples one day after testing, and dimensions were measured (Figure 1d). These cubes were smaller than specified in ASTM D3574 – 11 due to the low initial foam thickness [53]. Three cubes were cut from the stretched region of the gradient cuboid in Figure 1b to allow repeat testing of the only foam that was stretched during fabrication. Cubes were compression tested in all three orthogonal axes between platelets using the same equipment and settings as the tensile tests (Figure 2d & e) and a preload of 0.1 N to ensure contact, corresponding to 0.25 to 0.75% compression. Incremental Poisson's ratios were calculated by fitting linear trend lines to transverse vs. axial engineering strain data (from DIC, same system as tensile tests) at 0.5 or 1% axial strain increments, depending on the number of available data points for regression fitting. Incremental tangent moduli were calculated in the same way, from stress vs. axial engineering strain data from Instron's software Bluehill 4.0's force and displacement, and measured sample dimensions. Young's moduli were taken as the tangent moduli at the lowest calculated axial strain (up to 0.5 or 1%).

To see cell shapes, micro-computed tomographic (micro-ct) scans of ~5 × 5 × 20 mm samples from each region of each type of foam were collected (SkyScan 1172; 360° rotation, image acquisition every 1.4°, resolution <5 μm). Micro-ct data were rendered (SkyScan, CTVox) and images taken of one cell (~100 to 500 μm) deep volumes in each orthogonal axis. To help compare cell structures, single cell images were processed by removing unconnected pixels with areas under 2% of the cell using erosion functions (*imclose* and *bwareaeopen*) in MATLAB® 2019a (Mathworks, USA).

2.3. Analytical Modelling

Analytical models based on 2D cell projections [40], and the effect of air pressure based on analysis of the same polyethylene foam of lower density (LD-24, Zotefoam) [51], were combined and adapted. The adapted model was used to explain Young's moduli (E_y and E_z) and Poisson's ratios (ν_{yz} and ν_{zy}) at 0.75% compression and tension (ε_y and ε_z). The value of $\pm$ 0.75% strain was selected as the 2nd data point in most Tangent moduli and Poisson's ratio vs. strain data. Details of the model for 2D cell projections, taken from previous open cell foam work [40], are included as Supplementary Material S2, with unitless dimensions relative to the vertical rib length (*h = 1, which is diagonal rib length*). Some changes to cell dimensions were made from the previous study [40]. As low cell wall thickness is common in closed cell foams [41,51], relative rib/wall thickness was halved from 0.2, as used in the previous open cell foam work [40], to 0.1 (Figure S6). Cell walls were partially constrained by gas pressure; increasing the relative amount of stretching, rather than flexure and hinging, as discussed elsewhere [51]. With the support from the internal air pressure, rather than reducing the flexure and hinging constant (k_{hf}) for the thinner walls, k_{hf} was increased from 0.04 [40] to 0.10 in tension. Cell walls of unconverted closed cell foam begin to buckle at low (0 to 3%) compression [51]. Since many of the converted foams had kinked cell walls from fabrication, buckling was expected to occur at close to 0% compression, so k_{hf} was reduced three-fold (to 0.03) in compression, which was an arbitrary amount found to fit the data. Sensitivity to variations in k_{hf} are shown in the supplementary material (Figure S5). The force constants for flexing and hinging were unchanged from the previous model (0.04 and 0.0044, respectively) [40]. To account for gas pressure, relative volumetric deformation (Equation 1) was [51,52]:

$$\varepsilon_v = \frac{\varepsilon_u}{(1-\varepsilon_u-R)} \quad \textbf{(1)}$$

where relative density (R) was the density of polyethylene (~900 kg/m^3 [51]) divided by the measured foam density, and ε_v and ε_u were volumetric and uniaxial strains, respectively. The contribution of air pressure (p_{air}) to Young's modulus (E_{air}, Equation 2) was [51]:

$$E_{air} = \frac{p_{air}}{\varepsilon_u} = \frac{\varepsilon_v * p_0 * (1-2\nu)}{\varepsilon_u} \quad \textbf{(2)}$$

where p_0 was air pressure inside cells before testing, which was assumed to be atmospheric pressure (100 kPa) [51]. The foam modulus ($E_{combined}$) was calculated by adding the gas pressure contribution from Equation (2) and cellular modulus (E_{cell}) from Equation (S5) [51].

$$E_{combined} = E_{PE} * E_{cell} + E_{air} \quad \textbf{(3)}$$

where E_{PE} was the Young's modulus of polyethylene (300 MPa) [51]. Values for E_y and E_z were normalised to E_y from the analytical model at 0% strain and multiplied by the mean of measured compressive and tensile E_y. The combined Poisson's ratio ($\nu_{combined}$) was:

$$\nu_{combined} = \nu_{cell} + \nu_{fluid} * \frac{E_{air}}{E_{trans-cell}} \quad \textbf{(4)}$$

where ν_{cell} was the cellular Poisson's ratio contribution (ν_{cell}, Equation S6), ν_{fluid} was the Poisson's ratio of a fluid (of 0.5) and $E_{trans-cell}$ was the cellular transverse Young's modulus. Estimating the effect of trapped gas on Young's modulus and Poisson's ratio, rather than calculating its effect on cell rib deflection, means this analytical model can only show trends at low strains (< 1%).

3. Results

3.1 Sample measurements

Foam density increased (from 50.2 $\pm$ 0.8 kg/m^3, mean $\pm$ standard deviation (S.D.)) for the steamed samples following fabrication, giving FDRs between ~3 and 4 (**Figure 3**a). Density was unchanged (FDR = 1.0) for the dry heated region of foam that was not exposed to steam (in Figure 1c). Change in mass after a week in ambient conditions, before any other testing, was negligible (up to 0.3%), indicating any trapped water had evaporated and any increase in sample density was likely due to a decrease in volume. Unconstrained regions (FDR between 3.5 and 4.0) shrank more after fabrication than constrained regions (FDR between 3.0 and 3.5).

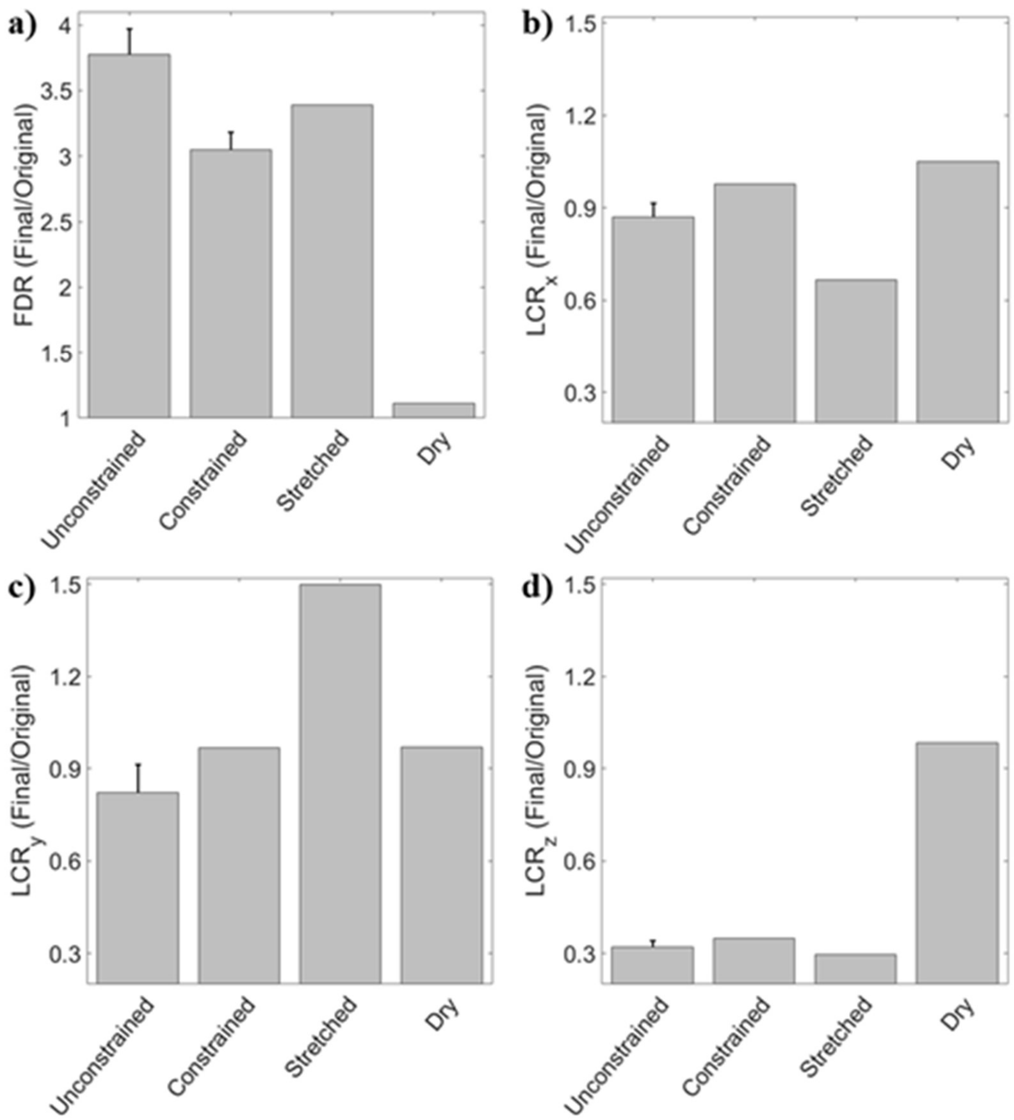

Figure 3. a) Final density ratio of samples cut for tensile testing and; b) to d) linear compression ratios measured from whole processed samples, parallel to the b) x-axis (shorter side), c) y-axis (longer side), and d) z-axis (through thickness). Same legend (d) for all. Error bars show 1 S.D. for conditions where multiple samples were fabricated.

Considering the unconstrained, steamed foam samples and regions, planar (x and y) LCRs (Figure 3b & c) were about 0.9, with more through thickness shrinking ($LCR_z \approx 0.3$, Figure 3d). The constrained region of the gradient sheet exhibited planar LCRs of 1.0 (i.e. unchanged, due to the constraints) and an LCR of 0.3 through thickness. The stretched region of the steamed cuboid retained its applied LCR of ~1.5 in its y-axis (Figure 3c), an LCR of 0.7 in the x-axis (Figure 3b) and similar through thickness LCR to other samples ($LCR_z \approx 0.3$, Figure 3d).

3.2 Cell Structures

There was negligible difference in cell structure between orientations for the unconverted foam (**Figure 4**a to c), suggesting little to no elongated cell rise [41], as expected [49]. Steam contraction in the unconstrained sheet (Figure 4d & e) reduced cell size and imparted different topology, corresponding to some kinks in the previously straight cell walls, which were most obvious through thickness (Figure 4d). The structure of cells on the outer faces of samples barely changed following fabrication, as cells on the outer faces were partially open from cutting and could not trap steam (Figure 4f). Constraining foam in two directions created a similar effect to the unconstrained conversion, except the cells were wide, with low thickness (Figure 4g), but similar to the unconverted foam (Figure 4a to c) in the constrained x-y plane (Figure 4h) and on their outer faces (Figure 4i). Stretching foam in the y-axis also produced a similar effect, with wider, thinner cells still (Figure 4g), and different topology, corresponding to some kinked cell walls in the x-y plane (Figure 4k), caused by contraction in the x-axis ($LCR_x = 0.7$, Figure 3b). The outer faces of steamed samples had hexagonal cells, which were longer in their stretched y-axis for samples stretched by pins during fabrication (Figure 4l).

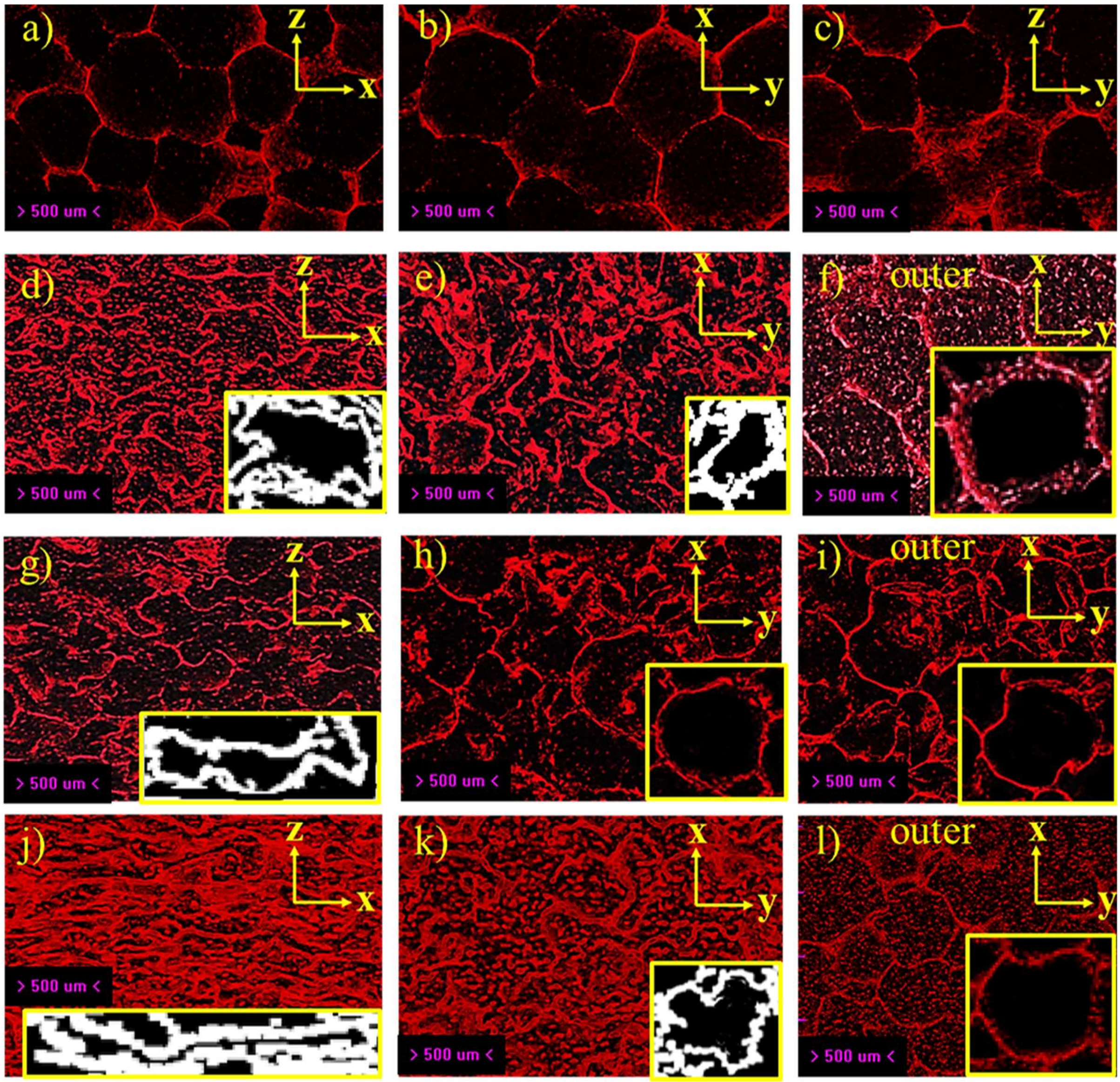

Figure 4. Micro-ct scans of a) to c) unconverted foam; d) to f) unconstrained, steamed sheet sample, g) to i) the constrained region of the constrained sheet, j) to l) the stretched region of the partially stretched gradient cuboid. Labels show orientation, subfigures f), i) and l) show steamed foam's outer face. Inserts in d) to l) show processed single cell images digitally expanded by 1.5 times their original size. White single cell images were processed in MATLAB®, others by minor manual editing to accentuate cell walls.

3.3 Digital Image Correlation

Contour plots of transverse strain from DIC show the unconverted foam contracted transversely at 2 and 10% tension (**Figure 5**a & b) and the auxetic foam expanded (Figure 5c & d). Contour plots at 10% compression show the unconverted foam expanded transversely (Figure 5e). The auxetic sample contracted transversely at the centre (Figure 5f) and expanded along the edges; corresponding to regions with (Figure 4g) and without (Figure 4i) re-entrant cell structures, respectively. See supplementary video for strain mapping of uniform and gradient samples in tension.

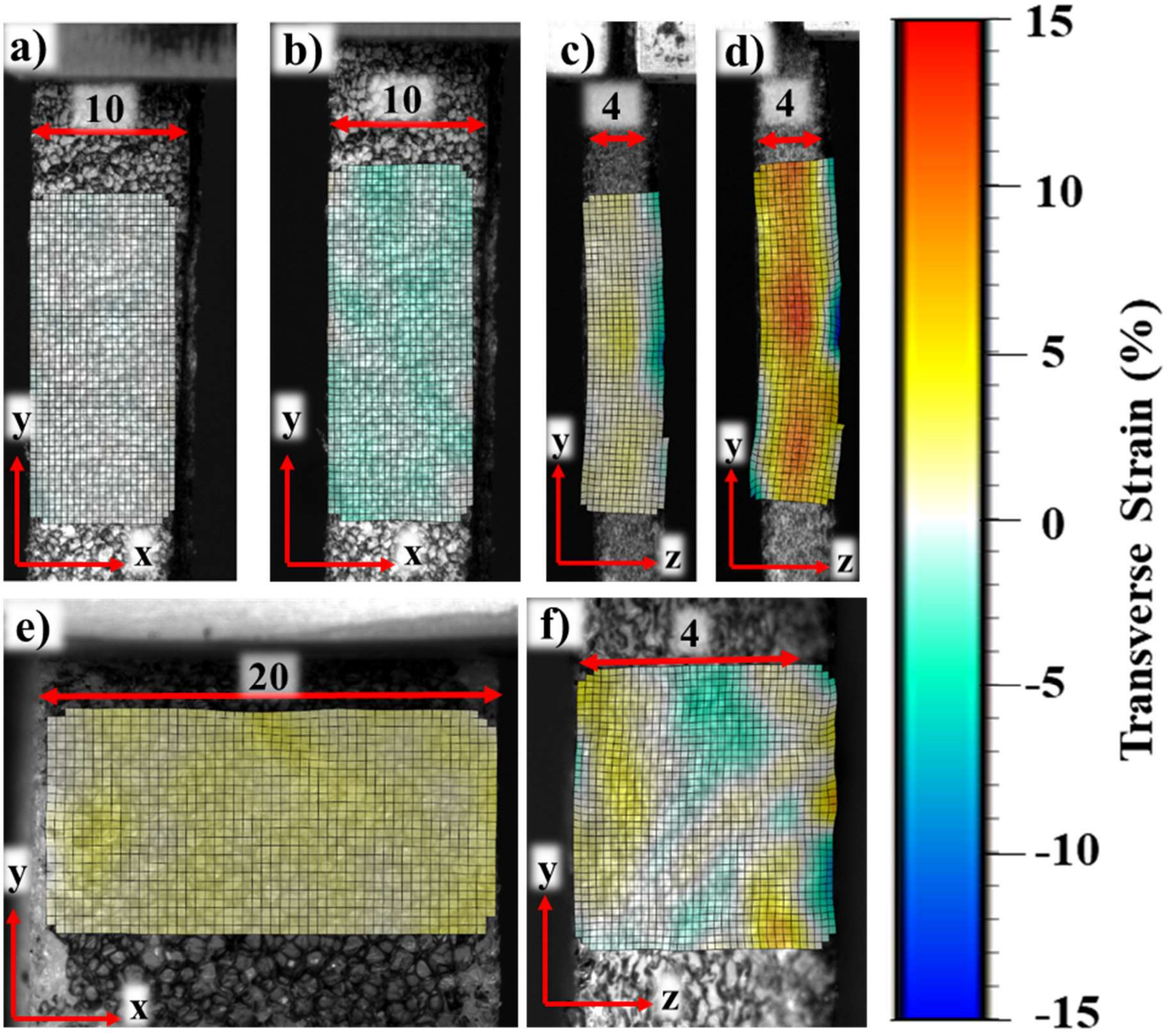

Figure 5. Contour plots of transverse strain from DIC of a) and b) unconverted foam at a) 2% and b) 10% tension; c) and d) the constrained region of the gradient sheet at c) 2% and d) 10% tension; e) unconverted foam at 10% compression; f) the constrained region of the gradient sheet at 10% compression. Labelled dimensions are in mm.

3.4 Stress and lateral strain vs. axial strain

NPR behavior (i.e. contraction) of the unconstrained foam was retained to ~2 to 3% compression (**Figure 6a**), followed by transverse expansion. The constrained region of the gradient sheet had a steeper compressive axial vs. transverse strain relationship and therefore a higher magnitude of (negative) Poisson's ratio than the unconstrained region. NPR was, however, only maintained to ~1% compression in the constrained region. Tensile transverse vs. axial strain was quasi-linear for all samples (Figure 6b), with the constrained region of the gradient sheet expanding more transversely than the unconstrained region. The unconverted foam exhibited transverse expansion in compression (Figure 6a) and transverse contraction (Figure 6b) in tension.

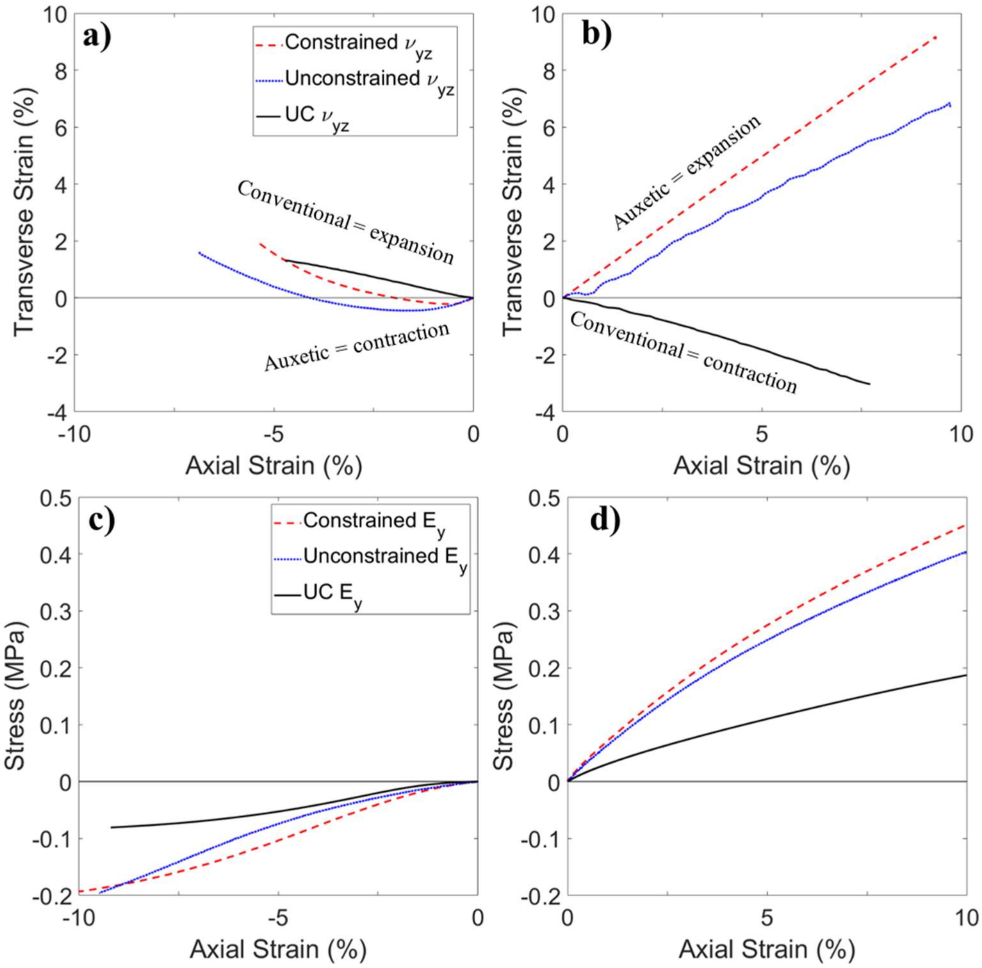

Figure 6. Sample plots of a) & b) Transverse vs. axial strain in a) compression and b) tension; c) & d) Stress vs. axial strain for constrained and unconstrained regions of the gradient sheet, and the unconverted foam in c) compression and d) tension. Negative strain values indicate axial compression and transverse contraction. Same legend applies to a) & b), and c) & d).

The unconverted foam exhibited its characteristic stress vs. strain plateau at ~5% compression [41,49,55] (Figure 6c). The constrained region of the gradient sheet also had a stress vs. strain plateau, at ~8% compression, and a steeper initial gradient and therefore higher Young's modulus than both the unconverted and unconstrained regions. The unconstrained region exhibited linear stress vs. strain of steeper gradient than the unconverted foam. In tension (Figure 6d), stress vs. strain relationships of all samples were quasi-linear, with the same order of low to high Young's moduli as in compression (unconverted < unconstrained < constrained).

3.5 Poisson's ratios

The unconverted sample was isotropic ($\nu \approx 0.4$, **Figure 7a & b**, Supplementary Material S1). Measured Poisson's ratios and tangent moduli of test samples cut from unconstrained regions of different fabricated samples were similar to each other (Figures S1 & S2). A selection of samples, from the constrained and stretched regions of gradient foams, demonstrating the different mechanical behaviors and imparted cell structures are outlined here. Detailed results are included in the supplementary material (Figures S1 & S2), along with collated Young's modulus and Poisson's ratio data (Supplementary Table S1). The mechanical properties of the dry heated region of foam were similar to the unconverted foam (Figures S1 & S2), as FDR and LCRs were ≈ 1, so cell structures were unchanged (Figure 3).

Concerning the gradient sheet, tensile and low strain (<0.5%) compressive Poisson's ratios of the unconstrained section were as low as -0.7 (ν_{yz}, Figure 7a & b). In the slightly compressed in-plane directions (LCR ≈ 0.9), Poisson's ratios ($\nu_{xy} \approx 0.1$) were lower than for the unconverted foam. During through thickness compression tests, ν_{zy} was about zero. In the unconstrained foam section (Figure 7c & d), Poisson's ratio had greater anisotropy; NPR reached a higher magnitude ($\nu_{yz} \approx -1.0$), whereas the in-plane Poisson's ratio was closer to that of the unconverted foam ($\nu_{xy} \approx 0.2$). Through thickness compressive Poisson's ratio (ν_{zy}) was also close to zero (Figure 7c). Trends in the stretched region (Figure 7e & f) were broadly similar to the constrained region, but the positive Poisson's ratio ν_{yz} (of 1) was higher in compression; as in similar work stretching open cell foam during fabrication [38,40].

Calculated Poisson's ratios, based on Equation (4) and schematics in Supplementary Figure S3, show reasonable agreement (within ~1 S.D.) with measured values (Figure 7 & Supplementary Material S2). The analytical model predicts that the effect of transverse expansion of gas in compression increases with cell anisotropy (Supplementary materials Figure S4 -S8), as does Figure 7 data. NPR (ν_{yz}) was present up to 2 to 3% compression for the unconstrained region (Figure 7a) and 1 to 2% for the constrained region (Figure 7c), whereas the stretched foam had positive compressive Poisson's ratio (Figure 7e).

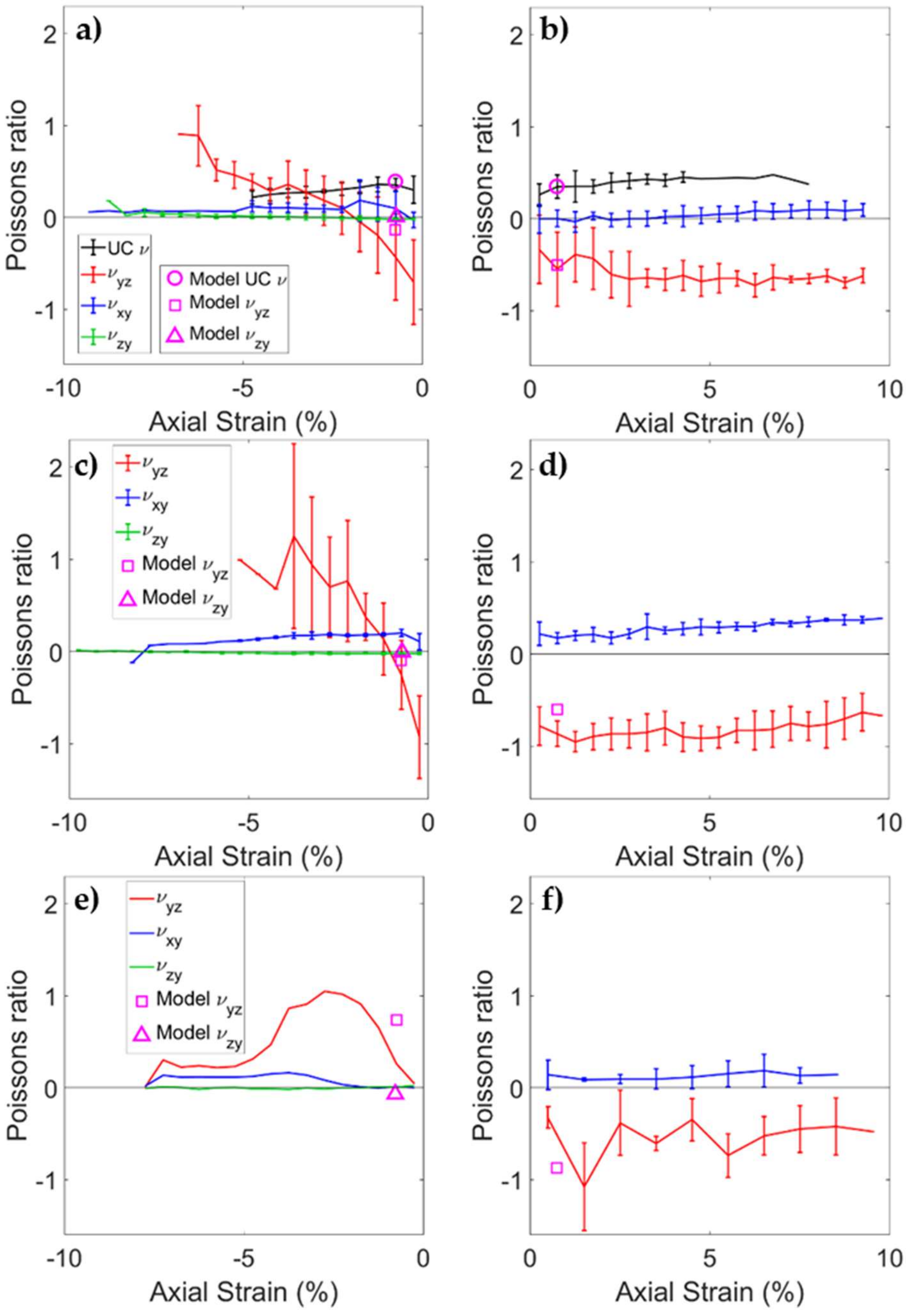

Figure 7. Measured and calculated (Equation 4) Poisson's ratio vs. axial strain for; a) & b) unconverted and unconstrained foam (samples from the gradient sheet, a) in compression, b) in tension), c) & d) constrained foam from the gradient sheet (c) in compression, d) in tension), e) & f) the stretched section of the gradient cuboid sample (e) in compression, f) in tension). Data for axial and transverse strain parallel to the x and y-axis or at 45° were combined. Mean values and error bars showing 1 S.D. are plotted, except for in (e) where median values were plotted in compression. Legends in a), c) & e) apply to b), d) & f), respectively. All samples and orientations are included in Supplementary material S1 and data is also included in Table S1.

3.6 Tangent moduli

Unconverted foam exhibited tangent moduli of ~1 MPa up to ~5% compression (**Figure 8**a), with a reduction to ~0.5 MPa when it entered the plateau region (Figure 6c), and of ~2.5 MPa up to 10% tension (Figure 8b). In compression, both regions of the gradient sheet (Figures 8a & c) were stiffer through thickness ($E_y \approx 2.5$ MPa at 5% compression) than in plane (E_x & $E_y \approx 1$ to 1.5 MPa). Planar tensile Young's moduli were lower in the unconstrained region (E_x & $E_y \approx 7$ MPa, Figure 8b) than the constrained region (E_x & $E_y \approx 8$ MPa, Figure 8d). Compressive tangent moduli parallel to the x and y-axis tended to be higher in the constrained region (~1 to 2 MPa, Figure 8c) than the unconstrained region (~0.5 to 1.5 MPa, Figure 8a), but lower (both ~1 to 2 MPa) when loaded parallel to the z-axis. When loaded along the stretched (y) axis, the stretched region of the gradient cuboid was stiffer (Figure 8e & f) than other orientations and samples; both in compression (tangent modulus up to 4 MPa, Figure 8e) and tension ($E_y \approx 12$ MPa, Figure 8f), agreeing with trends in previous work stretching open cell foam during fabrication [40,56]. Young's moduli are also in Supplementary Table S1.

Differences in both tensile and compressive tangent moduli between regions agree with increased anisotropy in Poisson's ratio measurements (Figure 7), micro-ct images of cell structures (Figure 4), LCRs (Figure 3) and the analytical model (Figure 8). Equation 3 also predicts Young's moduli to within ~1 S.D. of the mean measured value (Figure 8). As with Poisson's ratio measurement and calculations, the lower stiffness in tension supports increased cell wall flexure and bending in compression.

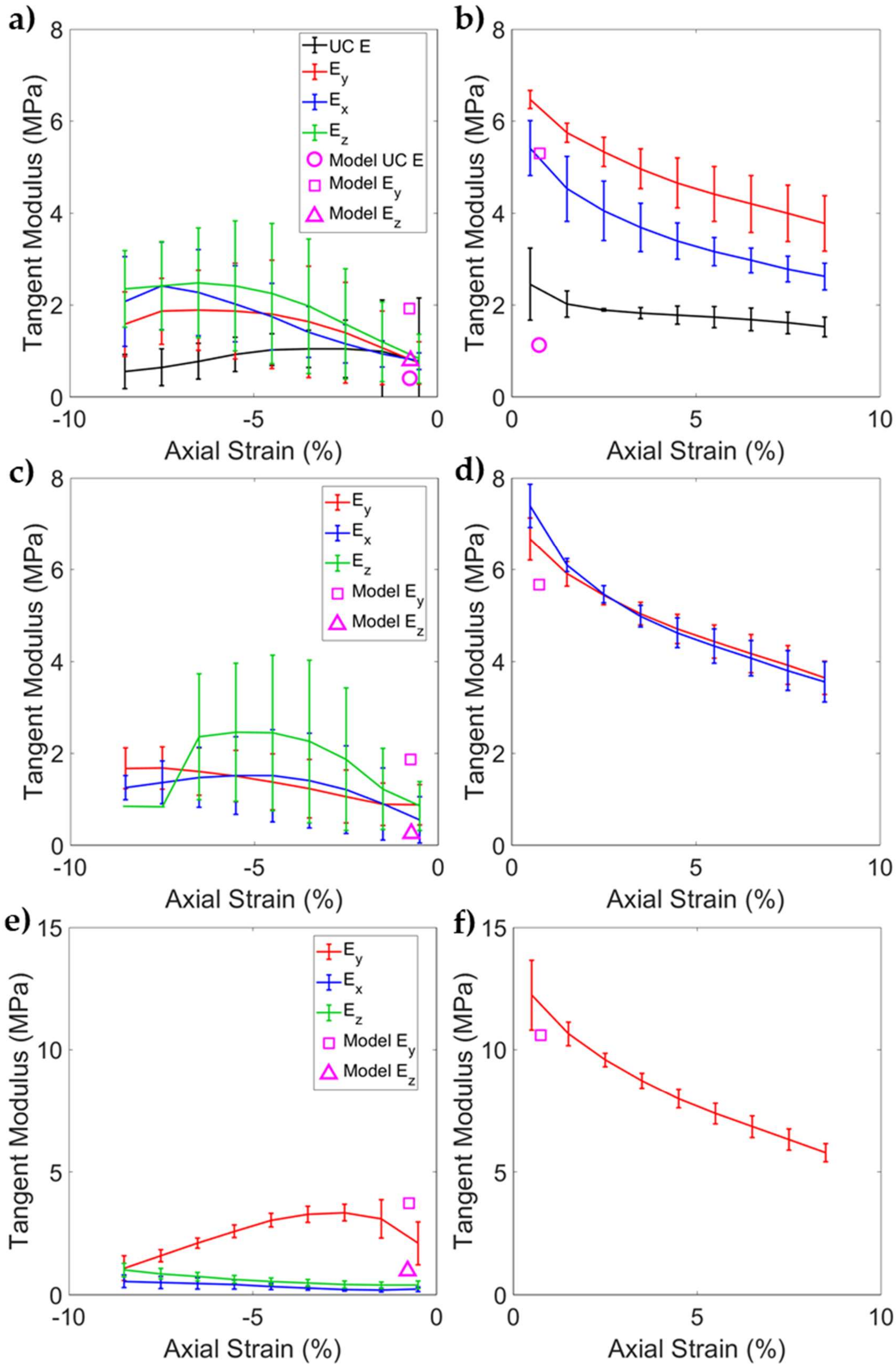

Figure 8. Mean and calculated (Equation 3) tangent moduli of a) & b) unconstrained and unconverted foam (samples from the gradient sheet) in a) compression and b) tension; c) & d) the constrained section of the gradient sheet in c) compression and d) tension; e) & f) the stretched section of the gradient cuboid in e) compression and f) tension. Error bars show 1 S.D. All samples and fabrication shown in Supplementary material S1, and data is replicated in Table S1.

4. Discussion

Constraining, stretching or preventing steam from reaching regions of closed cell foam allowed control over cell structure during steam conversions (Figure 3). Constraining and stretching foam regions during fabrication increased anisotropy in gradient foam regions. Comparison with an analytical model, adapted from previous works [40,51], showed agreement (within ~ 1 S.D.) between imparted LCRs (Figure 3) and cell structures (Figure 4), with measured Poisson's ratios (Figure 7) and Young's moduli (Figure 8). The imparted cell structures of regions of auxetic foam that were unconstrained during fabrication look similar to those in previous work, and agree with an analytical model [48,49]. Further work could steam larger and thicker samples of constrained foam, to allow for compression tests that comply with ASTM D3574 – 11 [53].

Regions of foam unconstrained during fabrication, from different samples, exhibited similar mechanical properties, including Poisson's ratios (lowest $\nu_{yz} \approx -0.7$, Figure 7, Figure S1) and tensile Young's moduli of ~7 MPa (Figure 8b, Figure S2). The gradient sheet had a slight gradient along its y-axis (e.g. $\nu_{yz} \approx -0.7$ to -0.8, tensile $E_y \approx 7$ to 8 MPa), as expected and predicted by the analytical model (Figures 7c, 7d, 8 c, 8d). The two cuboids had clear gradients between regions: i) Unconstrained regions were similar (e.g. $\nu_{yz} \approx -0.7$, tensile $E_y \approx 7$ MPa); ii) The stretched region had similar tensile ν_{yz} of ~-0.5 (Figures 7c) but higher tensile E_y of ≈ 12 MPa (Figure 8f); iii) The dry-heated region was similar to the unconverted foam (Figures 7a, 7b, 8a, 8b), with $\nu \approx 0.4$ and $E \approx 2.5$ MPa (Figures S1f and S2f).

The effects of modifying cell structure agreed with our understanding of open and closed cell foam, including: i) analytical models of auxetic and conventional open cell foam [40,41,50]; ii) analytical models of conventional closed cell foam [41,51,52], and; iii) previous tests of auxetic closed cell foam [47–49]. Cell structure (Figure 4h) and Poisson's ratio (Figure 7a & b) in directions constrained (LCRs = 1), but not stretched, by pins during steaming were similar to that of the unconverted foam. Young's moduli of the converted foam did, however, tend to increase with foam density from shrinkage in the unconstrained through thickness direction (Figures 3a, 8a & 8b). Kinked cell walls and smaller cells imparted by the steam process (Figure 4e & f) gave NPR (Figure 7a & b) and increased Young's modulus (Figure 8a & b), as in previous work with open cell foam [19,23,38,40].

Considering the gradient sheet, constraining the foam (and cells) during fabrication, and volumetric shrinking during cooling - when the polyethylene was softened by the remaining heat – is likely to have increased the diagonal rib length (i.e. *l* in Figure S3). Increasing the relative diagonal cell wall length in the analytical model increased transverse strain ($\varepsilon_{transverse}$ α l/h, whereby h is vertical rib length, Supplementary Figure S3) and the magnitude of cellular NPR (ν_{yz}, Figure S7a), agreeing with mechanical test data and clearest in tension (e.g. Figure 7a to d). The increased magnitude of NPR would, then, be expected to increase volumetric deformation, and therefore changes in internal air pressure, increasing stiffness ($E_{combined}$ α E_{air} α ε_v, Equation 2), as in Figure 8a to d [51].

Compressive and tensile characteristics of the steamed foams differed, depending on the specifics of fabrication. NPR was maintained to higher tension (10%) than compression (~2%, Figure 7), suggesting more implications for fit of personal protective equipment, and prosthetics, than indentation or impact performance, although this was not tested specifically. Previous work suggested that cell wall buckling began at low (0 to 3%) compression of closed cell foams [51]. The analytical model (Equations 3 & 4) predicts negative tensile Poisson's ratio (ν_{yz}), but near zero or positive compressive Poisson's ratio (ν_{yz}, Figure 7), and reduced compressive stiffness (E_y, Figure 8), as cell walls buckle. Lengthening cells, by stretching foam in the y-axis during fabrication (Figure 4j), increased stiffness in the y-axis (E_y, Figure 8e & f) [23,57], and gave positive compressive Poisson's ratio (Figure 7e).

Before considering internal air pressure, the analytical model and previous work in open cell foam [40], suggest compressive NPR, and low compressive transverse stiffness, as cell wall flexure and bending increase (Figure S5, [40]). With their low transverse stiffness, air trapped in the cells caused transverse expansion and positive compressive Poisson's ratio (Figure 7 and Equation 4). The effect of air pressure in the closed cells, and the compression level at which positive Poisson's ratio occurred (Figure 7a, c & e), increased with the diagonal cell wall length (Supplementary Figure S3 b to d), as relative transverse stiffness decreased (Figure 8) [40]. Further work could develop this auxetic closed cell foam analytical model for larger strains.

Unlike most auxetic open cell foams, the closed cell auxetic foams reported here had similar compressive stiffness (~1 to 4 MPa, Figure 8a) to foam in personal protective equipment (~1 MPa [58–60]), running shoe midsoles (~2 MPa [33,61]) liners for prosthetic sockets (~1 MPa [62]) and expanded foam in helmets (~5 to 20 MPa [63–65]). Foams fabricated herein also had a wide range of tensile moduli (5 to 12 MPa, Figure 8), similar to that of expanded foam used in helmets. These foams were up to twice as stiff as similar foam fabricated without constraints [49]. While similar stiffness open cell auxetic foams have been fabricated before [31], these closed cell auxetic foams have higher porosity (FDRs up to 5, Figure 3, than FDR ≈ 10 in previous work [31]), and high magnitude NPR during loading in the same axes as their desirable Young's moduli (~1 to 12 MPa, Figures 7 & 8). Alignment of desirable characteristics (NPR and Young's modulus), and high porosity, mean these auxetic closed cell foams could realise the previously demonstrated [4–6,8,28,37,66] and discussed [30,67–69] benefits of NPR to energy absorption [33,51,58–60,62–65]. The presented methods facilitate further development and testing, including impact testing at different temperatures and humidities, of auxetic and gradient foam for often discussed [1,19,30,68], but unrealised, applications for auxetic foam.

5. Conclusions

We demonstrate control over compression and cell structure during auxetic closed cell foam fabrications. Poisson's ratios between -1 and 1, compressive tangent moduli from 1 to 4 MPa and tensile Young's moduli between 5 and 12 MPa were shown within a gradient sample. Obtained mechanical properties agree (within ~1 S.D.) with analytical models adapted from previous models for auxetic open cell and conventional closed cell foam. Open cell gradient auxetic foam is available, but typically with Young's moduli at least ten times lower than that of the closed cell foams presented here. Now that such control is possible during closed cell auxetic and gradient foam fabrications, prototype devices featuring auxetic and gradient foam, such as sporting personal protective equipment, helmets, prosthetics and footwear, can be developed and tested. Future work could impact test the foams developed here for such applications. The development of an analytical model for auxetic closed cell foam provides a better understanding of such foams, which could help in their application to sports equipment and other devices.

6. Acknowledgements

The work was funded by Manchester Metropolitan University's Strategic Opportunities Fund, and Sheffield Hallam University's Creating Knowledge Investment Platform. Characterisation, testing, writing and analysis was under taken by Dr. Duncan, with equal guidance given by both co-authors.

7. References

1. Lakes RS. Foam Structures with a Negative Poisson's Ratio. Science (80-). 1987.235(4792). 1038–40.
2. Cross TM, Hoffer KW, Jones DP, Kirschner PB, Meschter JC. Auxetic Structures And Footwear With Soles Having Auxetic Structures (US 2015/0075034 A1). Vol. 1. 2015.
3. Moroney C, Alderson A, Allen T, Sanami M, Venkatraman P. The Application of Auxetic Material for Protective Sports Apparel. Proceedings. 2018.2(6). 251.
4. Chan N, Evans KE. Indentation resilience of conventional and auxetic foams. J Cell Plast. 1998.34. 231–60.
5. Lakes RS, Elms K. Indentability of conventional and negative Poisson's ratio foams. J Compos Mater. 1993.27(12). 1193–202.
6. Ge C. A comparative study between felted and triaxial compressed polymer foams on cushion performance. J Cell Plast. 2013.49(6). 521–33.
7. Lisiecki J, Błazejewicz T, Kłysz S, Gmurczyk G, Reymer P, Mikułowski G. Tests of polyurethane foams with negative Poisson's ratio. Phys Status Solidi Basic Res. 2013.250(10).

1988–95.

8. Allen T, Shepherd J, Hewage TAM, Senior T, Foster L, Alderson A. Low-kinetic energy impact response of auxetic and conventional open-cell polyurethane foams. Phys Status Solidi Basic Res. 2015.9. 1–9.
9. Scarpa F, Ciffo LG, Yates JR. Dynamic properties of high structural integrity auxetic open cell foam. Smart Mater Struct. 2003.13(1). 49–56.
10. Scarpa F, Pastorino P, Garelli A, Patsias S, Ruzzene M. Auxetic compliant flexible PU foams: Static and dynamic properties. Phys Status Solidi Basic Res. 2005.242(3). 681–94.
11. Scarpa F, Giacomin J, Zhang Y, Pastorino P. Mechanical performance of auxetic polyurethane foam for antivibration glove applications. Cell Polym. 2005.24(5). 253–68.
12. Li Q, Yang D. Vibro-acoustic performance and design of annular cellular structures with graded auxetic mechanical metamaterials. J Sound Vib [Internet]. 2020.466. 115038. Available from: https://doi.org/10.1016/j.jsv.2019.115038
13. Li Q, Yang D. Vibration and Sound Transmission Performance of Sandwich Panels with Uniform and Gradient Auxetic Double Arrowhead Honeycomb Cores. Shock Vib. 2019.2019.
14. Howell B, Prendergast P, Hansen L. Examination of acoustic behavior of negative poisson's ratio materials. Appl Acoust. 1994.43(2). 141–8.
15. Almutairi MM, Osman M, Tlili I. Thermal Behavior of Auxetic Honeycomb Structure: An Experimental and Modeling Investigation. J Energy Resour Technol Trans ASME. 2018.140(12).
16. Innocenti P, Scarpa F. Thermal conductivity properties and heat transfer analysis of Multi-re-entrant auxetic honeycomb structures. J Compos Mater. 2009.43(21). 2419–39.
17. Chun Checn H, Scarpa F, Hallak Panzera T, Farrow I, Peng H-X. Shear stiffness and energy absorption of auxetic open cell foams as sandwich cores. Phys Status Solidi. 2018.256(1). 1–9.
18. Timoshenko SP, Goodier JN. Theory of Elasticity. 3rd ed. New York: McGraw-Hill, USA; **1970**.
19. Alderson A, Alderson KL, McDonald SA, Mottershead B, Nazare S, Withers PJ, et al. Piezomorphic materials. Macromol Mater Eng. 2013.298(3). 318–27.
20. Evans KE. The design of doubly curved sandwich panels with honeycomb cores. Compos Struct. 1991.17(2). 95–111.
21. Chan N, Evans KE. Fabrication methods for auxetic foams. J Mater Sci. 1997.32. 5945–53.
22. Li Y, Zeng C. Room-Temperature, Near-Instantaneous Fabrication of Auxetic Materials with Constant Poisson's Ratio over Large Deformation. Adv Mater. 2016.28(14). 2822–6.
23. Sanami M, Alderson A, Alderson KL, McDonald S a., Mottershead B, Withers PJ. The production and characterization of topologically and mechanically gradient open-cell thermoplastic foams. Smart Mater Struct. 2014.23(5). 055016.
24. Lowe A, Lakes RS. Negative Poisson's ratio foam as seat cushion material. Cell Polym. 2000.19(3). 157–67.
25. Stojmanovski Mercieca LA, Formosa C, Grima JN, Chockalingam N, Gatt R, Gatt A. On the Use of Auxetics in Footwear: Investigating the Effect of Padding and Padding Material on Forefoot Pressure in High Heels. Phys Status Solidi Basic Res. 2017.254(12). 1–5.
26. Allen T, Duncan O, Foster L, Senior T, Zampieri D, Edeh V, et al. Auxetic foam for snow-sport safety devices. Snow Sport Trauma Saf Proc Int Soc Ski Saf. 2016.21.
27. Foster L, Peketi P, Allen T, Senior T, Duncan O, Alderson A. Application of Auxetic Foam in Sports Helmets. Appl Sci. 2018.8(3). 354.
28. Duncan O, Foster L, Senior T, Alderson A, Allen T. Quasi-static characterisation and impact testing of auxetic foam for sports safety applications. Smart Mater Struct. 2016.25(5). 054014.
29. Critchley R, Corni I, Wharton JA, Walsh FC, Wood RJK, Stokes KR. A review of the manufacture, mechanical properties and potential applications of auxetic foams. Phys Status Solidi Basic Res. 2013.250(10). 1963–82.
30. Duncan O, Shepherd T, Moroney C, Foster L, Venkatraman PD, Winwood K, et al. Review of auxetic materials for sports applications: Expanding options in comfort and protection. Appl Sci. 2018.8(6). 941.
31. Zhang Q, Lu W, Scarpa F, Barton D, Lakes RS, Zhu Y, et al. Large stiffness thermoformed open cell foams with auxeticity. Appl Mater Today. 2020.20. 100775.

32. Ankrah S, Mills NJ. Analysis of ankle protection in Association football. Sport Eng. 2004.7(1). 41–52.
33. Mills NJ, Fitzgerald C, Gilchrist A, Verdejo R. Polymer foams for personal protection: Cushions, shoes and helmets. Compos Sci Technol. 2003.63(16). 2389–400.
34. Mills NJ. The biomechanics of hip protectors. Proc Inst Mech Eng H. 1996.210(4). 259–66.
35. Duncan O, Clegg F, Essa A, Bell AMT, Foster L, Allen T, et al. Effects of Heat Exposure and Volumetric Compression on Poisson's Ratios, Young's Moduli, and Polymeric Composition During Thermo-Mechanical Conversion of Auxetic Open Cell Polyurethane Foam. Phys Status Solidi. 2019.
36. Grima JN, Attard D, Gatt R. A novel process for the manufacture of auxetic foams and for the conversion of auxetic foam to conventional form (WO 2010049511 A2). 2010. 1–5.
37. Lisiecki J, Klysz S, Blazejewicz T, Gmurczyk G, Reymer P. Tomographic examination of auxetic polyurethane foam structures. Phys Status Solidi Basic Res. 2013.251(2). 314–20.
38. Alderson A, Davies PJ, Alderson KIML, Smart GM. The Effects of Processing on the Topology and Mechanical Properties of Negative Poisson's Ratio Foams. Proc IMECE2005 2005 ASME Int Mech Eng Congr Expo Proc IMECE200. 2005. 1–8.
39. Bianchi M, Scarpa F, Banse M, Smith CW. Novel generation of auxetic open cell foams for curved and arbitrary shapes. Acta Mater. 2011.59(2). 686–91.
40. Duncan O, Allen T, Foster L, Senior T, Alderson A. Fabrication, characterisation and modelling of uniform and gradient auxetic foam sheets. Acta Mater. 2017.126. 426–37.
41. Gibson LJ, Ashby MF. Cellular solids. Structure and properties. **1997**. 67, 176–183, 259–264, 286, 301, 498 p.
42. Imam S, Driscoll H, Winwood K, Venkatraman P, Allen T. Efficacy of Density in Predicting the Protective Properties of Padded Clothing in Rugby †. Proc 13th Conf Int Sport Eng Assoc. 2020.49(38). 1–7.
43. Mills NJ. Foam protection in sport. In: Jenkins M, editor. Materials in sports equipment. Volume 1. Cambridge, UK: Woodhead Publishing Limited; **2003**. p. 20–9.
44. Mawkhlieng U, Majumdar A. Soft body armour. Text Prog. 2019.51(2). 139–224.
45. Sterzing T, Custoza G, Ding R, Cheung JTM. Segmented midsole hardness in the midfoot to forefoot region of running shoes alters subjective perception and biomechanics during heel-toe running revealing potential to enhance footwear. Footwear Sci. 2015.7(2). 63–79.
46. Mohsenizadeh S, Ahmad Z, Alipour R, Majid RA, Prawoto Y. Quasi Tri-Axial Method for the Fabrication of Optimized Polyurethane Auxetic Foams. Phys Status Solidi. 2019.1800587. 1800587.
47. Martz EO, Lee T, Lakes RS, Goel VK, Park JB. Re-entrant transformation methods in closed cell foams. Cell Polym. 1996.15(4). 229–49.
48. Fan D, Li M, Qiu J, Xing H, Jiang Z, Tang T. Novel Method for Preparing Auxetic Foam from Closed-Cell Polymer Foam Based on the Steam Penetration and Condensation Process. ACS Appl Mater Interfaces. 2018.
49. Duncan O, Birch A, Allen T, Foster L, Hart J, Alderson A. Effect of steam conversion on the cellular structure, Young's modulus and negative Poisson's ratio of closed cell foam. Smart Mater Struct. 2020.((Accepted)).
50. Masters IG, Evans KE. Models for the elastic deformation of honeycombs. Compos Struct. 1996.35(4). 403–22.
51. Mills NJ, Zhu HX. The high strain compression of closed-cell polymer foams. J Mech Phys Solids. 1999.47(3). 669–95.
52. Rusch KC. Load-compression behavior of brittle foams. J Appl Polym Sci. 1970.14(5). 1263–76.
53. Annual Book of ASTM Standards. Standard Test Methods for Flexible Cellular Materials — Slab , Bonded , and Molded Urethane Foams. Annual Book of ASTM Standards 2008.
54. Wang D, Diazdelao FA, Wang W, Lin X, Patterson EA, Mottershead JE. Uncertainty quantification in DIC with Kriging regression. Opt Lasers Eng. 2016.78. 182–95.
55. Mills NJ, Gilchrist A. Modelling the indentation of low density polymer foams. Cell Polym. 2000.19(6). 389–412.
56. Ramaswamy H. Fabrication and testing of 2-dimensional Z-expandable auxetic textile

structures for impact protective clothing applications. 2014. 1–15.
57. Allen T, Hewage T, Newton-Mann C, Wang W, Duncan O, Alderson A. Fabrication of Auxetic Foam Sheets for Sports Applications. Phys Status Solidi Basic Res. 2017.1700596. 1–6.
58. Signetti S, Nicotra M, Colonna M, Pugno NM. Modeling and simulation of the impact behavior of soft polymeric-foam-based back protectors for winter sports. J Sci Med Sport. 2018.
59. Nicotra M, Moncalero M, Messori M, Fabbri E, Fiorini M, Colonna M. Thermo-mechanical and impact properties of polymeric foams used for snow sports protective equipment. Procedia Eng. 2014.72. 678–83.
60. Ankrah S, Mills NJ. Performance of football shin guards for direct stud impacts. Sport Eng. 2003.6(4). 207–19.
61. Verdejo R, Mills NJ. Heel-shoe interactions and the durability of EVA foam running-shoe midsoles. J Biomech. 2004.37(9). 1379–86.
62. Sanders JE, Greve JM, Mitchell SB, Zachariah SG. Material properties of commonly-used interface materials and their static coefficients of friction with skin and socks. J Rehabil Res Dev. 1998.35(2). 161–76.
63. Krundaeva A, De Bruyne G, Gagliardi F, Van Paepegem W. Dynamic compressive strength and crushing properties of expanded polystyrene foam for different strain rates and different temperatures. Polym Test. 2016.55(2016). 61–8.
64. Mosleh Y, Bosche K Vanden, Sloten J Vander, Verpoest I, Ivens J. Combined shear-compression test to characterize foams under oblique loading for bicycle helmets. In: In Proceedings of the 16rd European Conference on Composites Materials ECCM16, Seville, Spain. **2014**. p. 22–6.
65. Andena L, Caimmi F, Leonardi L, Ghisi A, Mariani S, Braghin F. Towards Safer Helmets: Characterisation, Modelling and Monitoring. Procedia Eng. 2016.147. 478–83.
66. Pastorino P, Scarpa F, Patsias S, Yates JR, Haake SJ, Ruzzene M. Strain rate dependence of stiffness and Poisson's ratio of auxetic open cell PU foams. Phys Status Solidi Basic Res. 2007.244(3). 955–65.
67. Novak N, Vesenjak M, Ren Z. Auxetic cellular materials - A review. Stroj Vestnik/Journal Mech Eng. 2016.62(9). 485–93.
68. Evans KE, Alderson A. Auxetic materials: Functional materials and structures from lateral thinking! Adv Mater. 2000.12(9). 617–28.
69. Yang W, Li ZM, Shi W, Xie BH, Yang MB. On auxetic materials. J Mater Sci. 2004.39(10). 3269–79.

Supplementary Material

Fabrication, characterisation and analytical modelling of gradient auxetic closed cell foams

Olly Duncan[1*], Andrew Alderson[2], Tom Allen[1],

[1] *Department of Engineering, Faculty of Science & Engineering, Manchester Metropolitan University, John Dalton Building, Chester Street, Manchester M1 5GD, UK.*
[2] *Materials and Engineering Research Institute, Faculty of Arts, Computing, Engineering and Sciences, Sheffield Hallam University, Howard Street, Sheffield S1 1WB UK.*
* Corresponding author (Email: O.Duncan@mmu.ac.uk)

All figures with 'S' proceeding number are in supplementary information, all figures and equations without the preceding 'S' are from the manuscript. All figures to be printed available in colour, all citations refer to reference list in the manuscript.

S1. Detailed Mechanical Properties

Table S1: Young's modulus and Poisson's ratios of all samples in Figures 7 & 8. Data is taken from the closest point to 0% compression or tension.

	Characteristic	***Unconverted***	***Unconstrained***	***Constrained***	***Stretched***
Compression	ν_{yz}	0.30 ± 0.15	-0.70 ± 0.46	-0.93 ± 0.45	0.04
	ν_{xy}		-0.03 ± 0.08	0.11 ± 0.09	0.00
	ν_{zy}		-0.02 ± 0.01	-0.02 ± 0.01	0.02
	E_y (MPa)	0.77 ± 1.38	0.74 ± 0.46	0.88 ± 0.44	2.10 ± 0.88
	E_x (MPa)		0.78 ± 0.18	0.55 ± 0.50	0.23 ± 0.09
	E_z (MPa)		0.83 ± 0.53	0.89 ± 0.53	0.41 ± 0.15
Tension	ν_{yz}	0.26 ± 0.12	-0.33 ± 0.37	-0.78 ± 0.21	-0.32 ± 0.11
	ν_{xy}		0.00 ± 0.15	0.22 ± 0.13	0.14 ± 0.16
	E_y (MPa)	2.61 ± 0.58	6.47 ± 0.20	6.67 ± 0.46	12.22 ± 1.43
	E_x (MPa)		5.41 ± 0.60	7.40 ± 0.47	

Poisson's ratios of unconverted samples were isotropic (**Figure S**1a & b), and therefore agreed with values in the manuscript (Figure 7a & b). Poisson's ratios were also similar to the dry heated section of foam (**Figure S**1e & f). The Poisson's ratios of unconstrained, steamed sections of the half-steamed sample (**Figure S**1e & f) were similar to the unconstrained, steamed foam sections shown in the manuscripts (Figure 7a & b).

Tangent moduli of unconverted samples (**Figure S**2a & b) were isotropic, and therefore agreed with values in the manuscript (Figure 8a & b) and were similar to the dry heated section of foam (**Figure S**2e & f). The tangent moduli of the unconstrained, steamed section of the half-steamed sample (**Figure S**2e & f) were similar to the unconstrained, steamed foam sections shown in the manuscript (Figure 8a & b).

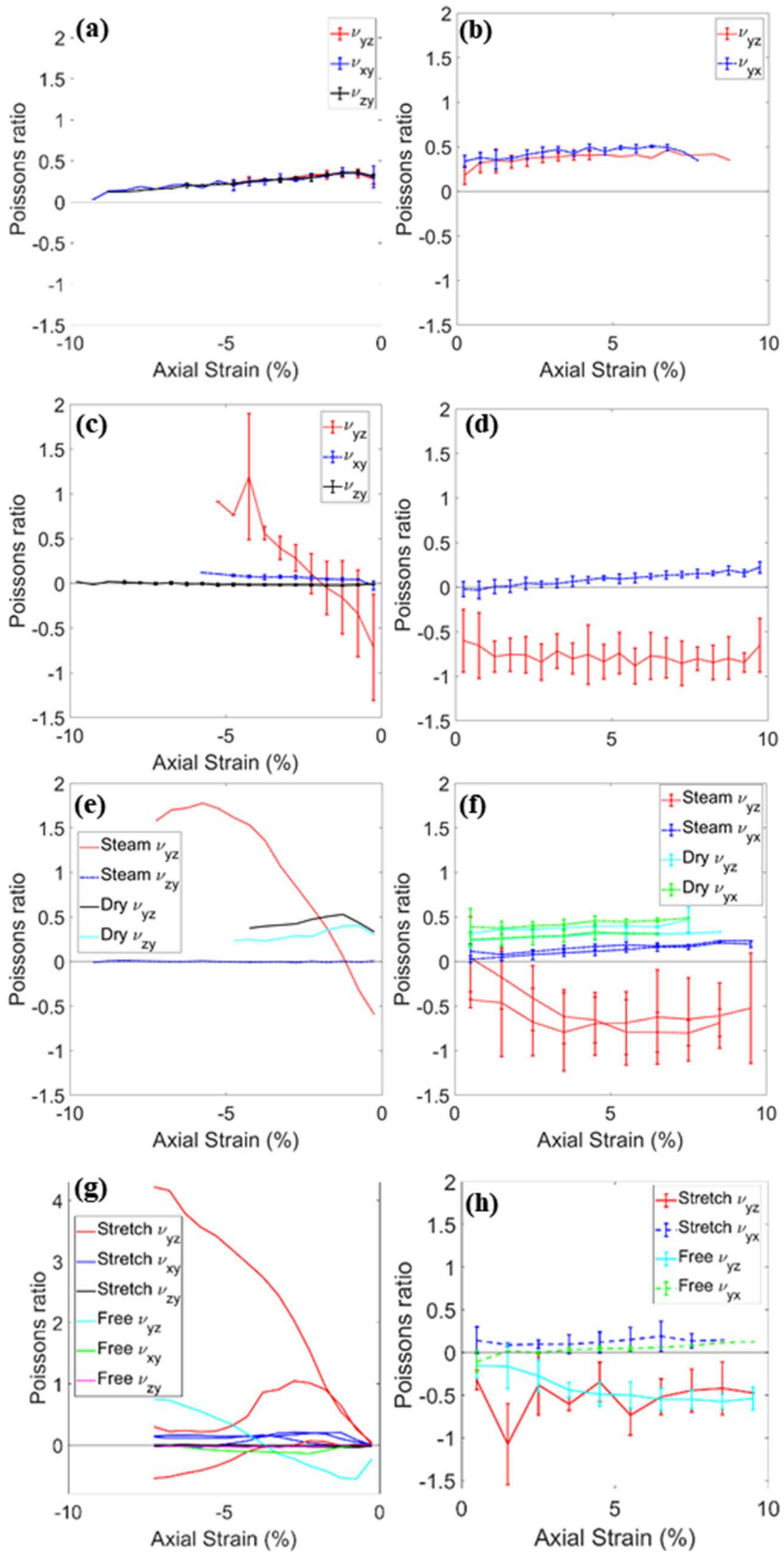

Figure S1. Poisson's ratio vs. axial strain for the; a) & b) unconverted foam in compression and tension (respectively); c) & d) the sheet steamed without constraints; e) & f) the half steamed, half dry-heated cuboid, and; g) and h) all sections of the stretched sample. All data for the sheets, (a) to (d), is plotted at 0.5% strain increments, all data for the cuboids, (e) to (h), is plotted at 1% strain increments. Where error bars are shown, data is mean and S.D.; where error bars are not shown, all tested samples are plotted.

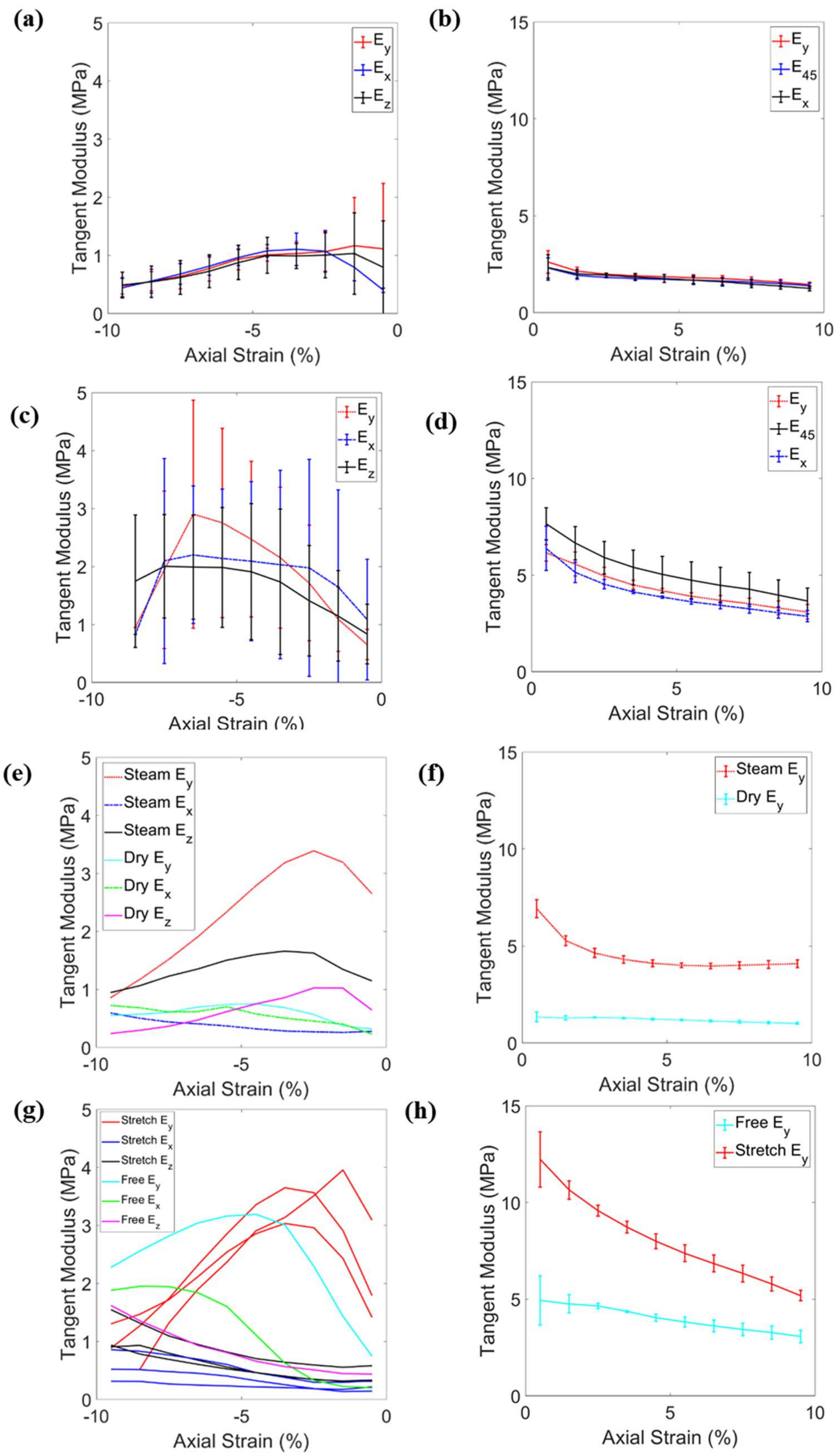

Figure S2. Tangent modulus vs. axial strain for the; a) & b) unconverted foam in compression and tension (respectively); c) & d) the sheet steamed without constraints; e) & f) the half steamed, half dry-heated cuboid, and; g) and h) all samples of the stretched sample. All data for the sheets, (a) to (d), is plotted at 0.5% strain increments, all data for the cuboids, (e) to (h), is plotted at 1% strain increments. Where error bars are shown, data is mean and S.D.; where error bars are not shown, all tested samples are plotted.

S2. Analytical Model Details

Poisson's ratio and Young's moduli, relative to cell wall angle, are described by Equations S1 to S4, taken from previous work [33].

$$\nu_{yz} = \frac{\sin\theta_{yz}\cos^2\theta_{yz}\left(\frac{1}{k_{hf}}-\frac{1}{k_s}\right)}{\left(\frac{h_{yz}}{l_{yz}}+\sin\theta_{yz}\right)\left[\frac{\sin^2\theta_{yz}}{k_{hf}}+\frac{\cos^2\theta_{yz}}{k_s}\right]} \quad \textbf{(S1)}$$

$$\nu_{zy} = \frac{\sin\theta_{yz}\left(\frac{h_{yz}}{l_{yz}}+\sin\theta_{yz}\right)\left(\frac{1}{k_{hf}}-\frac{1}{k_s}\right)}{\left[\frac{\cos^2\theta_{yz}}{k_{hf}}+\frac{2\frac{h_{yz}}{l_{yz}}+\sin^2\theta_{xz}}{k_s}\right]} \quad \textbf{(S2)}$$

$$E_y = \frac{\cos\theta_{yz}}{b_{yz}\left(\frac{h_{yz}}{l_{yz}}+\sin\theta_{yz}\right)\left[\frac{\sin^2\theta_{yz}}{k_{hf}}+\frac{\cos^2\theta_{yz}}{k_s}\right]} \quad \textbf{(S3)}$$

$$E_z = \frac{\left(\frac{h_{yz}}{l_{yz}}+\sin\theta_{yz}\right)}{b_{yz}\cos\theta_{yz}\left[\frac{\cos^2\theta_{yz}}{k_{hf}}+\frac{2\frac{h_{yz}}{l_{yz}}+\sin^2\theta_{yz}}{k_s}\right]} \quad \textbf{(S4)}$$

where h_{yz} is the vertical cell wall length, l_{yz} the diagonal cell wall length, k_s is the cell wall stretching force constant and b_{yz} is the cell wall thickness. Inputting values for the unconstrained and unconverted foams (FigureS3a & b), Equations S1 and S3 predict relatively high variation in Poisson's ratio and Young's modules as cell wall angle (θ_{yz}) and the flexure and hinging constant (k_{hf}) varies (**Figure S4**). Equations S5 to S7 were used to calculate the off-axis Young's modulus, Poisson's ratio and strain; with an offset angle $\Phi = 10^{\circ}$:

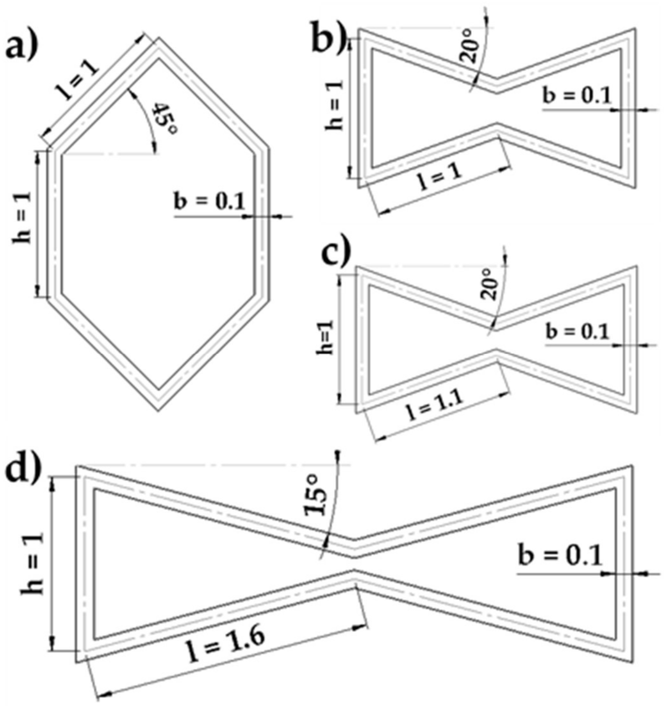

Figure S3. Schematics showing the y-z plane of a) unconverted, b) unconstrained, c) constrained and d) stretched cells (y across the page, z upwards) used in the analytical model.

$$E_y(\phi) = \left[\frac{\cos^4\phi}{E_y} + \cos^2\phi\,\sin^2\phi\left(\frac{1}{G_{yz}} - \frac{2\nu_{yz}}{y}\right) + \frac{\sin^4\phi}{E_z}\right]^{-1} \qquad \textbf{(S5)}$$

$$\nu_{yz}(\phi) = E_y(\phi)\left[\frac{(\cos^4\phi+\sin^4\phi)\nu_{yz}}{E_y} - \cos^2\phi\,\sin^2\phi\left(\frac{1}{E_y} + \frac{1}{E_z} - \frac{1}{G_{yz}}\right)\right] \qquad \textbf{(S6)}$$

$$\varepsilon_y(\emptyset) = ln\left(\frac{l_{yz}cos\,\theta_{yz} - \delta_{yz}sin\,\theta_{yz}}{l_{yz(0)}cos\,\theta_{yz(0)}}\right)cos^2\,\emptyset + \;ln\left(\frac{h_{yz}+l_{yz}sin\,\theta_{yz}+\delta_{yz}cos\,\theta_{yz}}{h_{yz(0)}+l_{yz(0)}sin\,\theta_{yz(0)}}\right)sin^2\,\emptyset \qquad \textbf{(S7)}$$

where G_{yz} is cell shear modulus, and δ_{yz} is the deflection of the diagonal cell wall due to flexing. Equations S8 to S12 were used to calculate changes in cell wall length, and transverse deflection. Equations S6 and S7 are for loading parallel to the y or z-axis, respectively.

$$G_{zy} = \left[\frac{b_{yz}\left(\frac{h_{yz}}{l_{yz}}\right)^2 \left(1+\frac{2h_{yz}}{l_{yz}}\right) cos\theta_{yz}}{K_{hf}\left(\frac{h_{yz}}{l_{yz}}+sin\theta_{yz}\right)} + \frac{b_{yz}\left(1+\frac{h_{yz}}{l_{yz}}sin\theta_{yz}\right)^2}{K_s \cos\theta_{xz}\left(\frac{h_{yz}}{l_{yz}}+sin\theta_{yz}\right)} \right]^{-1} \quad \textbf{(S8)}$$

$$l_{yz}^2 = -\frac{2K_h}{K_s} \ln\left(\frac{sin\theta_{yz}}{sin\theta_{yz(0)}}\right) + l_{yz(0)}^2 \quad \textbf{(S9)}$$

$$l_{zy}^2 = \frac{2K_h}{K_s} \ln\left(\frac{\cos\theta_{yz(0)}}{\cos\theta_{yz}}\right) + l_{yz(0)}^2 \quad \textbf{(S10)}$$

$$h_{yz} = h_{yz(0)} exp\left[\frac{2K_h}{l_{yz}^2 K_s} \ln\left(\frac{\sec\theta_{yz} + \tan\theta_{yz}}{\sec\theta_{yz(0)} + \tan\theta_{yz(0)}}\right)\right] \quad \textbf{(S11)}$$

$$\delta_{yz} = \frac{K_h}{K_f} \frac{(\theta_{yz} - \theta_{yz(0)})}{l_{yz}} + \delta_{yz(0)} \quad \textbf{(S12)}$$

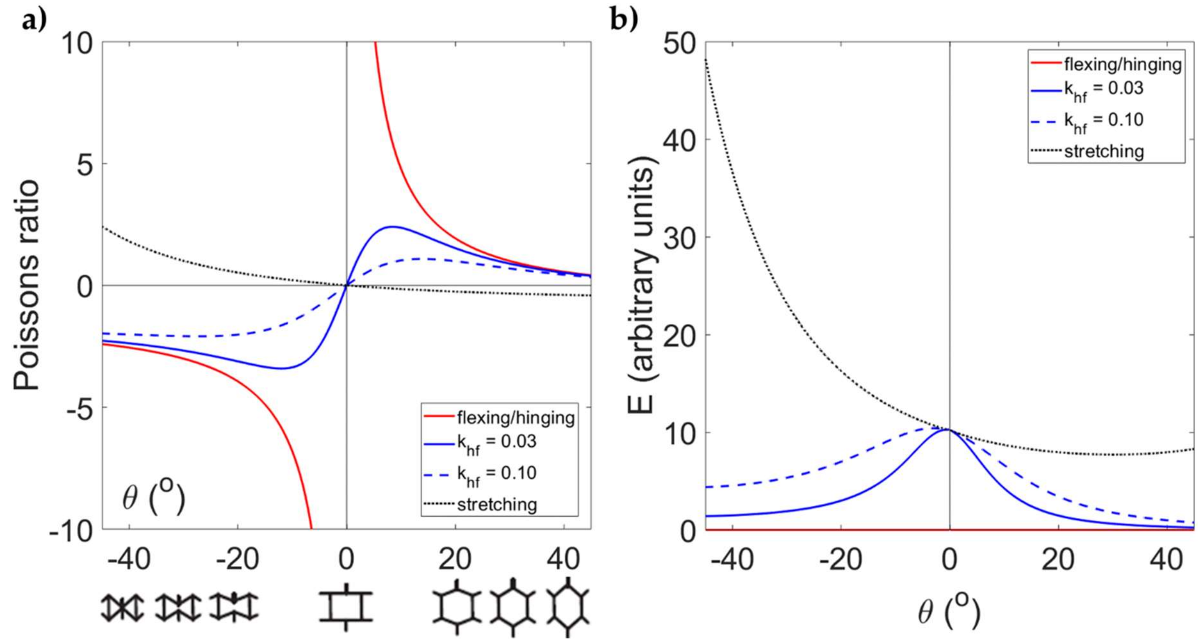

Figure S4. Poisson's ratio (ν_{yz}) vs. cell wall angle (Equation S1) and b) Young's modulus (E_y) v cell wall angle (Equation S3), for the foam cell structure, with no offset angle (Φ), h = l = 1 and b = 0.1, k_h = 0.0044, k_f = 0.04, k_s = 1, and variable values for the flexure and hinging force constant (k_{hf}).

Applying an offset angle $\Phi = 10^\circ$ (**Figure S5**), the Poisson's ratios vary less, and Young's moduli variation increases (Equations S5).

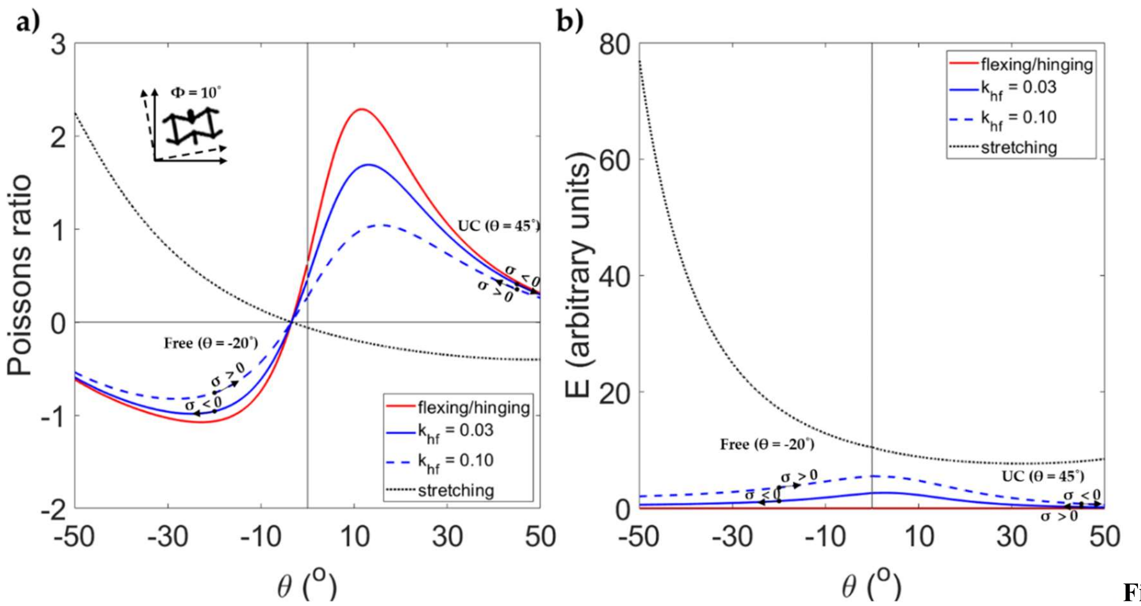

Figure S5. Poisson's ratio (ν_{yz}) vs. cell rib angle (Equation S6) and b) Young's modulus (E_y) v cell rib angle (Equation S5), for the foam cell structure, with an offset angle $\Phi = 10^{\circ}$, h = l = 1 and b = 0.1, $k_h = 0.0044$, $k_f = 0.04$, $k_s = 1$, and variable values for the flexure and hinging force constant (k_{hf}).

Reducing rib thickness, from 0.2 [33] in previous work to 0.1, to reflect the low thickness of closed cell walls [51], reduces the effect of cell rib angle on Young's modulus but does not change the Poisson's ratio from cellular deformation; assuming k_{hf} is unchanged (**Figure S6**). Reducing the effect of cell rib angle on Young's modulus could, though, increase the relative effect of air pressure on Poisson's ratio (Equation 4).

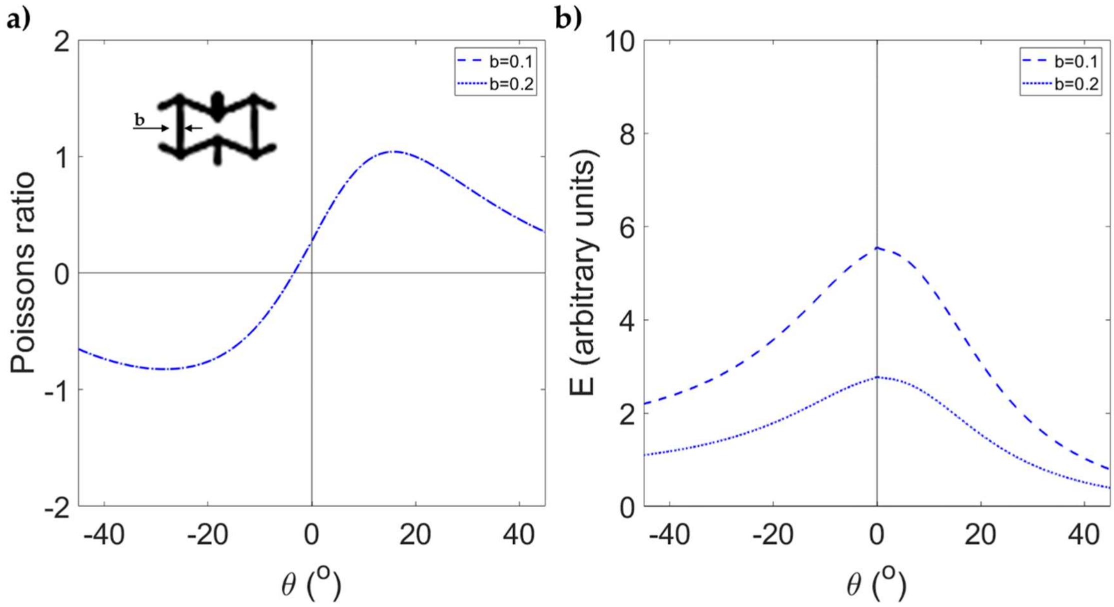

Figure S6. Poisson's ratio (ν_{yz}) vs. cell rib angle (Equation S6) and b) Young's modulus (E_y) v cell rib angle (Equation S5), for the foam cell structure, with an offset angle $\Phi = 10^{\circ}$, h = l = 1 and $k_{hf} = 0.1$, $k_h = 0.0044$, $k_f = 0.04$, $k_s = 1$, and variable values for cell wall thickness.

Increasing the length of the diagonal rib, to reflect imparted LCRs (Figure 3) and positive Poisson's ratio thinning of the cell walls with applied tension, and the cell structure images (Figure 4), for constrained and stretched foam regions (l = 1.1 and 1.6, Figures S3c & d), increases the magnitude of Poisson's ratios and Young's moduli (**Figure S7**)

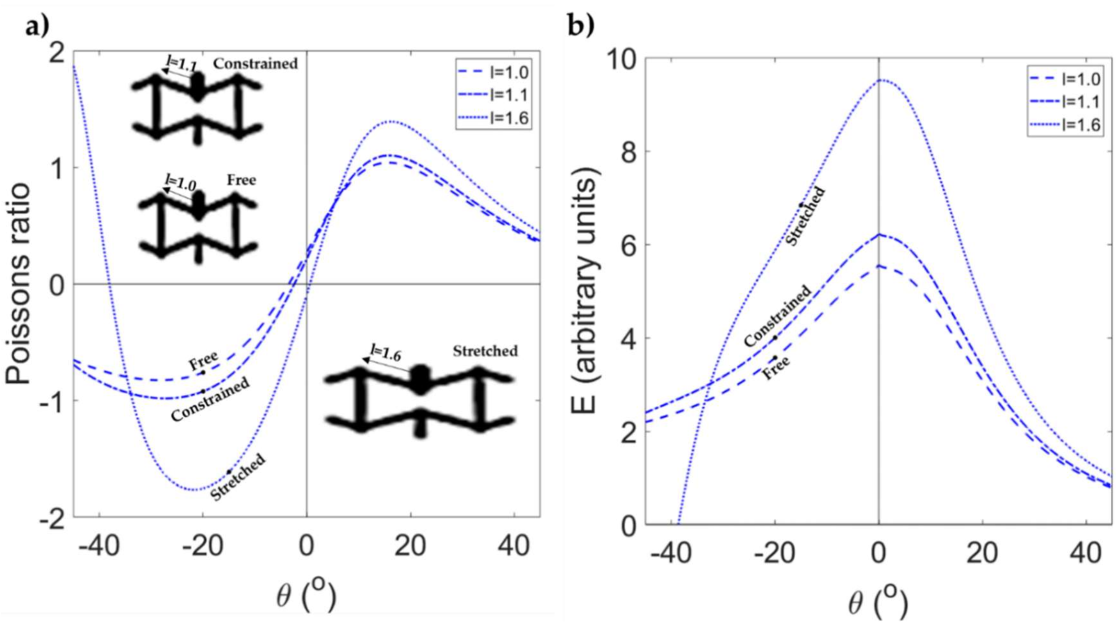

Figure S7. Poisson's ratio (ν_{yz}) vs. cell rib angle (Equation S6) and b) Young's modulus (E_y) v cell rib angle (Equation S5), for the foam cell structure, with an offset angle $\Phi = 10°$, h = 1 and $k_{hf} = 0.1$, b = 0.1, $k_h = 0.0044$, $k_f = 0.04$, $k_s = 1$, and variable values for diagonal cell wall length (l).

Reducing the flexure and hinging constant (k_{hf}) decreased compressive Poisson's ratio and Young's modulus calculated from cell dimensions (**Figure S8**). With the decreased Young's modulus in the transverse (z) axis, as shown in Figure 8 in the manuscript, combing cellular deformation with gas pressure (Equation 4) increased compressive Poisson's ratio, bringing the high negative values (dashed blue line) towards zero (black line), while still decreasing Young's modulus.

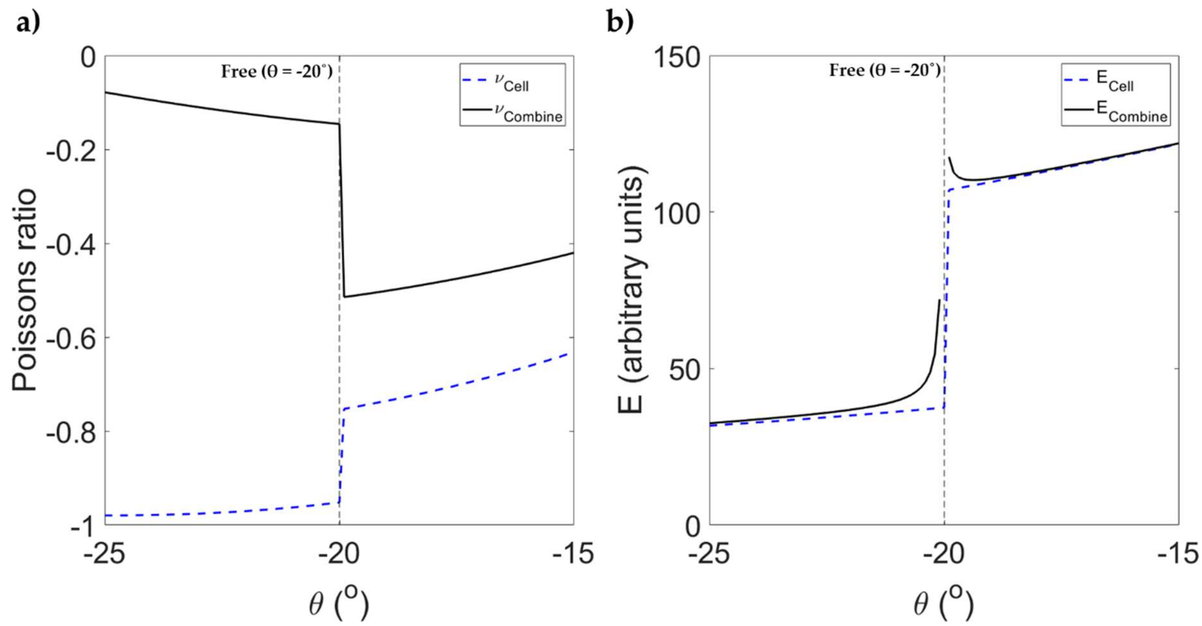

Figure S8. Poisson's ratio (ν_{yz}) vs. cell rib angle and b) Young's modulus (E_y) v cell rib angle, for the unconstrained, converted foam cell structure without (Equations S5 and S6) and with the effect of air pressure (Equations 3 and 4). Offset angle $\Phi = 10^{\circ}$, $h = l = 1$, $k_{hf} = 0.1$ in tension and 0.03 in compression, $b = 0.1$, $k_h = 0.0044$, $k_f = 0.04$, $k_s = 1$, $R = 0.8$, $p_0 = 100$ kPa, $E_{PE} = 300$ MPa.